Abstract of "Modeling of Ethylene-Vinyl Acetate (EVA) foam: Parametric studies of material properties and application to shoe midsoles"

by Leinani Cathryn Roylo, Degree Sc.M., Brown University, May 2022.

Ethylene-Vinyl Acetate (EVA) foam is a type of closed-cell elastomeric foam that consists of a polymeric elastomer matrix and air and is used in a wide variety of applications due to the material's ability to dissipate energy. Midsoles in shoes, for example, greatly benefit from the properties of foam as the dissipation of energy reduces the impact on people's feet during physical activity. Most existing constitutive models can only capture certain features of the mechanical behavior of foams during specific and limited loading conditions. As such, we focused on a recently-developed, nonlinear, large-deformation viscoelastic constitutive model for our studies due to its ability to capture mechanical responses in compression, over a wide range of strain rates, and in both loading and unloading. The first aim of this thesis focused on the material properties that appear in the constitutive model. We elucidated the role of selected material properties in the constitutive model through finite-element-based parametric studies of cyclic, uniaxial, compression-like deformation of a foam layer with a flat, circular indenter. The effects on the simulated response when varying both equilibrium and non-equilibrium material properties of the constitutive model as well as the loading frequency were studied. The second aim of this thesis was to apply the constitutive model to simulations of cyclic loading of a shoe midsole, specifically the geometry of the shoe midsole from Reebok's Zig line of shoes. This aim utilized a three-dimensional finite-element model to simulate compression of the midsole by a flat, circular indenter. The effects on the simulated response of the midsole when varying the frequency and position of the indenter were examined. The results when varying frequency were analogous to the baseline cases of the parametric studies in the first aim, and the results when varying position were affected by the geometry of the midsole, which dictated the dominant mode of deformation in the foam.

Modeling of Ethylene-Vinyl Acetate (EVA) foam: Parametric studies of material properties and application to shoe midsoles

by

Leinani Cathryn Roylo

Sc. B., Brown University, 2021

Submitted in partial fulfillment of the requirements for the

Degree of Master of Science in the School of Engineering at Brown University

Providence, Rhode Island

May 2022

This thesis by Leinani Cathryn Roylo is accepted in its present form
by the School of Engineering as satisfying the
thesis requirements for the degree of Master of Science.

Date ____________ ________________________________

David L. Henann, Ph.D., Advisor

Approved by the Graduate Council

Date ____________ ________________________________

Andrew G. Campbell, Ph.D.
Dean of the Graduate School

Curriculum Vitæ

Leinani Cathryn M. Roylo started her undergraduate study at Brown University in 2017, and after her first year, she knew that engineering was her passion. To become more involved in the engineering community, Leinani became a Peer Mentor for the design curriculum of the introductory engineering course the following year. Her responsibilities included facilitating groups of students with design projects and guided them in using various tools and machines in the Brown Design Workshop. After one semester, she was promoted to a Head Mentor, adding the duties of hiring, training, and supervising peer mentors while improving the design curriculum for the introductory engineering course. These improvements involved updating design projects to be more understandable, fulfilling, and doable, as well as strengthening the continuity between the lectures and this design curriculum. Since her promotion, Leinani remained in her Head Mentor position until she graduated.

While being a Head Mentor, Leinani was employed with other positions. One position was a Solids Mechanics grader, in which she graded students' homework assignments for the Solid Mechanics engineering course and ensured consistency amongst grading policies between her fellow graders. Another position was a Teaching Assistant for the Heat and Mass Transfer course. Leinani, again, graded students' homework assignments but also held office hours to enhance student learning throughout the semester. An additional responsibility was to conduct laboratory sessions that catered to all student needs in a hybrid-learning environment.

After graduating from Brown University in 2021 with a Bachelor of Science in Mechanical Engineering, Leinani interned at the W. M. Keck Observatory and worked on a mechanical engineering project for the summer of 2021. She defined requirements and conceptualized possible solutions in collaboration with Keck's mechanical engineering team and technicians to create a safer work environment for the technicians when they are working under a suspended mirror segment (1000 lb load). Leinani also designed and analyzed (FEA and hand calculations) a first iteration of a safety structure using SolidWorks, including identifying initial off-the-shelf parts and validating that the design exceeded the recommended factor of safety of five. Lastly, she presented the culmination of her work to the staff of the W. M. Keck Observatory and the Canada-France-Hawai‘i Telescope, describing the design process and justifying the recommendation of her final solution.

In the fall of 2021, Leinani enrolled again at Brown University's School of Engineering for one more year as part of Brown's Fifth-Year Masters Program. In her first semester, she had two jobs. The first one being a Homework Developer for the introductory engineering course, in which she developed weekly homework assignments and corresponding solutions in collaboration with the professors. Leinani's second job was a grading position for the Advanced Mechanics of Solids course, where she was the only person who graded students' homework assignments.

Lastly, Leinani focused on her research with Professor David Henann, Ph.D., during her second semester. The culmination of her work can be read in this paper. With her completion of coursework and her thesis, Leinani graduated in May 2022 with a Master of Science in Engineering: Mechanics of Solids.

Acknowledgements

First and foremost, I would like to express my deepest gratitude to my advisor, Professor David Henann, for his guidance and support throughout my research and thesis writing. Professor Henann was actually the one who convinced me to do a thesis during my master's program, and I would not change that decision if I were to do this all over again. I learned a lot throughout this journey that I will apply to both my professional and personal life. Thank you again to Professor Henann for this wonderful experience and for teaching me the basis of my solid mechanics knowledge.

Secondly, I would like to thank Reebok's 2021 Human Performance Engineering Team, particularly Beth Wilcox, Jason Leach, and Jake Vollmar, for meeting with us and providing information on their testing procedures, as well as, their Zig models. A special thank you to Jake for dedicating a lot of his time and energy in creating a workable mesh for the midsole. Chapter 3 would not have been possible without you!

Third, I would like to show my appreciation to Brown University's School of Engineering for providing me with great resources and a home for the past five years. The ERC, B&H, and BDW (thank you, Chris Bull) will forever hold a special place in my heart. Also, to all of my professors throughout my five years at Brown, thank you.

Lastly, I would like to show my love and appreciation to my family and friends who have supported me throughout my life ♡

To The Roylo ʻOhana

Contents

List of Tables **xiii**

List of Figures **xv**

1 Introduction **1**
1.1 Background on Foam Materials and Constitutive Modeling 1
1.2 Summary of the Large-deformation, Viscoelastic Constitutive Model 3
1.2.1 Equilibrium Response 4
1.2.2 Non-equilibrium Response 6
1.3 Thesis Contributions 10

2 The Effects of Material Parameters: Parametric Studies in Cyclic Indentation **13**
2.1 Simulation Details and Baseline Results 13
2.2 Equilibrium Material Parameters 16
2.2.1 Shear and Bulk Moduli 17
2.2.2 Volumetric Locking 19
2.3 Non-Equilibrium Material Parameters 21
2.3.1 Branch 1 22
2.3.2 Branches 2, 3, and 4 28

3 Application to Shoe Midsoles **33**
3.1 Simulation Details and Baseline Results 33
3.2 Varying Frequency at One Position 38
3.3 Varying Position at One Frequency 39

4 Conclusion **43**
4.1 Summary 43
4.2 Future Directions 45

A Force Versus Displacement Curves for Parametric Studies Involving Non-Equilibrium Newtonian Branches **47**

List of Tables

1.1 Equilibrium material parameters for the closed-cell EVA foam 6
1.2 Non-equilibrium material parameters for the closed-cell EVA foam 10

2.1 Values of m and correlating values of $\dot{\gamma}_0$ 22

List of Figures

1.1 A rheological schematic of the nonlinear, large-deformation, viscoelastic constitutive model. 3

2.1 Finite-element configuration for axisymmetric numerical simulations of cyclic indentation of a foam substrate. 14
2.2 Baseline force versus displacement curve for EVA foam under cyclic indentation at 3 Hz with displacement control. 16
2.3 Comparison of calculated dissipation efficiency under displacement and load control during cyclic indentation. 17
2.4 Force versus displacement curves during cyclic indentation when varying frequency and the ground-state moduli, G_0 and B. 18
2.5 Peak forces and dissipation efficiencies as a function of frequency during cyclic indentation when varying G_0 and B. 19
2.6 Force versus displacement curves during cyclic indentation when varying frequency and the volumetric locking parameter, J_{min}. 20
2.7 Peak forces and dissipation efficiencies as a function of frequency during cyclic indentation when varying J_{min}. 21
2.8 Force versus displacement curves during cyclic indentation when varying m. 23
2.9 Peak forces and dissipation efficiencies as a function of frequency during cyclic indentation when varying m. 24
2.10 Force versus displacement curves during cyclic indentation when varying G_{neq} for Branch 1. 26
2.11 Peak forces and dissipation efficiencies as a function of frequency during cyclic indentation when varying G_{neq} for Branch 1. 27
2.12 Peak forces and dissipation efficiencies as a function of frequency during cyclic indentation when varying G_{neq} for Branches 2, 3, and 4. 29

3.1 Configuration for numerical simulations of cyclic indentation of a shoe midsole with a view cut along the x-z-plane. 34
3.2 Top-view of the shoe midsole geometry and finite-element mesh. 34
3.3 Multiple views of the undeformed shoe midsole and indenter geometry and finite-element mesh 36
3.4 Contour plots of the von Mises effective stress and logarithmic strain invariants (K_1, K_2, and K_3) for the baseline case at an indenter displacement of 7 mm onto shoe midsole. 37
3.5 Force versus displacement curves during cyclic indentation of a shoe midsole when varying loading frequency at a fixed position. 39
3.6 Peak forces and dissipation efficiencies as a function of frequency during cyclic indentation of a shoe midsole at a fixed position. 39

3.7 Force versus displacement curves during cyclic indentation of a shoe midsole when varying the position of the indenter at 3 Hz. 40
3.8 Peak forces and dissipation efficiencies as a function of position during cyclic indentation of a shoe midsole at 3 Hz. 41

A.1 Force versus displacement curves during cyclic indentation when varying G_{neq} for Branch 2. 48
A.2 Force versus displacement curves during cyclic indentation when varying G_{neq} for Branch 3. 49
A.3 Force versus displacement curves during cyclic indentation when varying G_{neq} for Branch 4. 50

Chapter 1

Introduction

1.1 Background on Foam Materials and Constitutive Modeling

Ethylene-Vinyl Acetate (EVA) foam is a type of elastomeric foam that consists of a polymeric elastomer matrix and air [1–3]. The mechanical behavior of foam is controlled by the material properties of the elastomer matrix and the amount of air within the matrix, resulting in the material to be highly compressible with a strong coupling between the volumetric and distortional responses. Furthermore, the viscoelasticity of the matrix material allows foam to absorb greater amounts of energy than ordinary elastic materials for a certain stress-level and strain-rate. The ability to dissipate energy is why foams are commonly used in protective equipment, mattresses, padding, and packaging materials. Midsoles in shoes, for example, greatly benefit from the properties of foam as the dissipation of energy reduces the impact on people's feet as they do physical activity [1].

Many constitutive models have been created to capture the unique mechanical behavior of elastomeric foams used in a wide variety of applications. For the equilibrium, elastic response of foams, there are several modeling approaches for the free energy density function: phenomenological curve-fitting approaches that depend on the principal stretches [4–10], Blatz-Ko type hyperelasticity models [11–13] that are based on the principal invariants of the Cauchy-Green deformation tensor, hyperelastic modeling based on invariants of the logarithmic (Hencky) strain tensor [14], homogenization-based approaches [15–18] that consider porous elastomers with microstructures consisting of closed-cell pores, fully-micromechanical models based on strut-type unit cells [19–23], or unit cells involving cylindrical or spherical voids [18, 24, 25].

Elastomeric foams also have a rate-dependent mechanical behavior, in which researchers have decomposed that response into a time-independent hyperelastic part and a time-dependent viscoelastic part. There are typically two types of approaches for the time-dependent viscoelastic part. The first approach is a hereditary integral model, motivated by linear viscoelastic models and formulated in terms of relaxation or memory functions [e.g., 8, 26–29]. The second approach is a framework based on the multiplicative decomposition of the deformation gradient into elastic and inelastic parts [e.g., 9, 30–34].

Most existing models can capture certain features of the response of viscoelastic foams but are often only applicable to specific loading conditions, e.g., simple compression or only the loading portion of the response. However, applications often involve complex deformation histories with different modes of loading and variable loading rates. In particular, the studies presented in this thesis require a constitutive model that allows us to explore the mechanical behaviors of a foam that can be used in an application of a shoe. As a result, this thesis focused on the recent work of Li et al. [34], who presented a nonlinear, large-deformation viscoelastic constitutive model for foam materials that is summarized in the next section. This constitutive model was used for our studies because of its ability to capture mechanical responses in compression, over a wide range of strain rates, and in both loading and unloading. The model is complex and involves a number of material properties, so in the first aim of this thesis, we sought to understand the role of several important properties through finite-element-based parametric studies in cyclic indentation. Since Li et al. [34] calibrated and validated their model for EVA, which is a common foam

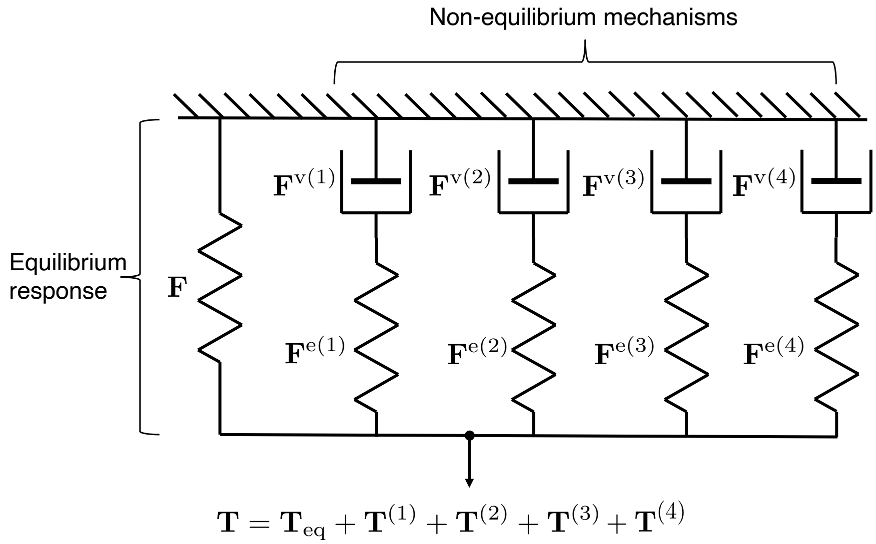

Figure 1.1: A rheological schematic of the nonlinear, large-deformation, viscoelastic constitutive model. The left branch represents the equilibrium response of the material, which is described by the hyperelastic model of Landauer et al. [14], and the non-equilibrium material response is described by four nonlinear, Maxwell-like, non-equilibrium mechanisms in parallel with the equilibrium branch. (Reproduced from Li et al. [34] with permission.)

material used in shoes, the second aim of this thesis was to apply the model to numerical simulations of shoe midsoles.

1.2 Summary of the Large-deformation, Viscoelastic Constitutive Model

In this section, we summarize the isotropic, viscoelastic model for large-deformation, rate-dependent behavior of elastomeric foams, recently developed by Li et al. [34], which will be the focus of this thesis. The constitutive model is based upon a decomposition of the response into an equilibrium hyperelastic response and a number of dissipative, non-equilibrium contributions, shown schematically in Figure 1.1. The left branch represents the equilibrium hyperelastic response of the material, which is described by the model introduced in Landauer et al. [14], and the non-equilibrium, rate-dependent material response is described by four nonlinear, Maxwell-like, non-equilibrium mechanisms in parallel with the equilibrium branch. Each mechanism is denoted by an integer index $\alpha \in \{1,2,3,4\}$.

The constitutive equations relate the following basic fields:[1] $\mathbf{x} = \chi(\mathbf{X},t)$, motion; $\mathbf{F} = \nabla\chi$, $J = \det\mathbf{F} > 0$, deformation gradient; $\mathbf{F} = \mathbf{RU} = \mathbf{VR}$, polar decomposition of $\mathbf{F}$; $\mathbf{V} = \sum_{i=1}^{3} \lambda_i \mathbf{l}_i \otimes \mathbf{l}_i$, spectral decomposition of $\mathbf{V}$; $\mathbf{E} = \sum_{i=1}^{3} (\ln \lambda_i)\mathbf{l}_i \otimes \mathbf{l}_i$, spatial logarithmic (Hencky) strain; $\mathbf{T}$, $\mathbf{T} = \mathbf{T}^\top$, Cauchy stress; ψ, free energy density per unit volume of reference configuration.

1.2.1 Equilibrium Response

The referential free-energy density ψ is additively decomposed into equilibrium and non-equilibrium contributions: $\psi = \psi_{\text{eq}} + \sum_{\alpha=1}^{4} \psi_{\text{neq}}^{(\alpha)}$, and the equilibrium hyperelastic response is specified through the free-energy density ψ_{eq}, which we take to depend on the invariants of the logarithmic strain tensor $\mathbf{E}$ as proposed by Criscione et al. [35], which are denoted as $\{K_1, K_2, K_3\}$. The first invariant $K_1 = \text{tr}\,(\mathbf{E}) = \ln(J)$ represents the amount of dilatation, and the second invariant $K_2 = |\text{dev}\,(\mathbf{E})| \geq 0$ is the magnitude of constant-volume distortion. The third invariant $K_3 = 3\sqrt{6}\det(\text{dev}\,(\mathbf{E})/K_2)$ represents the mode of constant-volume distortion and is constant for a given distortion mode, e.g., $K_3 = -1$ for simple compression, $K_3 = 0$ for simple shear, and $K_3 = 1$ for simple tension. The equilibrium contribution to the Cauchy stress is then obtained through the derivatives of the free-energy function $\psi_{\text{eq}} = \tilde{\psi}_{\text{eq}}(K_1, K_2, K_3)$ utilizing the chain rule and yielding [35]

$$\mathbf{T}_{\text{eq}} = J^{-1}\left[\frac{\partial \tilde{\psi}_{\text{eq}}}{\partial K_1}\mathbf{1} + \frac{\partial \tilde{\psi}_{\text{eq}}}{\partial K_2}\mathbf{N} + \frac{\partial \tilde{\psi}_{\text{eq}}}{\partial K_3}\frac{1}{K_2}\mathbf{Y}\right], \tag{1.1}$$

where $\mathbf{N} = \text{dev}\,(\mathbf{E})/K_2$ and $\mathbf{Y} = 3\sqrt{6}\mathbf{N}^2 - \sqrt{6}\mathbf{1} - 3K_3\mathbf{N}$.

Following Landauer et al. [14], we take the equilibrium free-energy density function

[1] *Notation:* The symbols ∇, Div and Curl denote the gradient, divergence, and curl with respect to the material point $\mathbf{X}$ in the reference configuration; grad, div, and curl denote these operators with respect to the point $\mathbf{x} = \chi(\mathbf{X},t)$ in the deformed configuration. We write $\text{tr}\,\mathbf{A}$, $\det\mathbf{A}$, $\text{dev}\,\mathbf{A}$, $\text{sym}\,\mathbf{A}$, and $\text{skw}\,\mathbf{A}$ to denote the trace, determinant, deviatoric part, symmetric part, and skew part of a tensor $\mathbf{A}$, respectively.

$\tilde{\psi}_{\text{eq}}(K_1, K_2, K_3)$ to be in the following form:

$$\tilde{\psi}_{\text{eq}}(K_1, K_2, K_3) = G_0 \left[X_{\text{eq}}(K_1) K_2^2 + L_{\text{eq}}(K_2, K_3) \right] + B f_{\text{eq}}(K_1), \tag{1.2}$$

where G_0 and B are the ground-state shear and bulk moduli, respectively, and the phenomenological functions appearing in (1.2) are summarized below.

1. The distortional/volumetric-coupling response function X_{eq}:

$$X_{\text{eq}}(K_1) = \frac{1}{2} \left(X_1' + X_2' \right) K_1 + \frac{\Delta_{\text{K}}}{2} \left(X_1' - X_2' \right) \ln \left[\frac{\cosh\left((K_1 - K_1^0)/\Delta_{\text{K}} \right)}{\cosh\left(K_1^0/\Delta_{\text{K}} \right)} \right] + 1. \tag{1.3}$$

   The function $X_{\text{eq}}(K_1)$ depends approximately linearly on K_1 but with different slopes before and after the onset of the plateau regime in compression. The parameter $K_1^0 < 0$ is the value of K_1 at which the transition to the plateau regime occurs, and $\Delta_{\text{K}} > 0$ is a parameter denoting the K_1-range of the transition to the plateau regime. The parameters X_1' and X_2' are the slopes of $X_{\text{eq}}(K_1)$ before and after the plateau regime in compression, respectively.

2. The higher-order distortional response function L_{eq}:

$$L_{\text{eq}}(K_2, K_3) = C_0 K_2^p + C_1 \left(1 + K_3\right) K_2^q, \tag{1.4}$$

   where $C_0 \geq 0$ and $C_1 \geq 0$ are constant parameters and $p > 2$ and $q > 2$ are higher-order exponents. The second term does not affect the response in compression ($K_3 = -1$) and allows for different higher-order responses in compression and tension.

3. The purely volumetric response function f_{eq}:

$$f_{\text{eq}} = \frac{J^{C_2} - C_2 \ln J - 1}{C_2^2} + \frac{C_3}{r-1} \left[\frac{-1}{J^{r-1}} + \frac{(1 - J_{\text{min}})^r}{(J - J_{\text{min}})^{r-1}} + J_{\text{min}} \right], \tag{1.5}$$

   where $J = \exp(K_1)$ is the volume ratio and J_{min}, r, C_2, and C_3 are constant parameters.

Equilibrium material parameters													
G_0 [kPa]	B [kPa]	$J_{\min}$	C_1	K_1^0	Δ_K	X_1'	X_2'	C_0	p	q	C_2	C_3	r
500	1000	0.16	1.2	-0.1	0.12	7	0.64	0.35	3	4	20	0.21	2

Table 1.1: Equilibrium material parameters for the closed-cell EVA foam, reported in Li et al. [34].

The parameter $J_{\min}$ represents the minimum allowable value of J, and df_{eq}/dK_1 diverges as J approaches $J_{\min}$ from above. The parameter $J_{\min}$ is in the range $0 < J_{\min} < 1$. The term involving C_2 in (1.5) captures the volumetric response in tension and prior to the plateau regime in compression, while the term involving C_3 accounts for the stiffening behavior in compression after the plateau regime.

The material parameters for the closed-cell EVA foam corresponding to the equilibrium response (estimated using simple compression/tension data at a low strain rate of $2 \times 10^{-4}\,\mathrm{s}^{-1}$ in Li et al. [34]) are shown in Table 1.1.

1.2.2 Non-equilibrium Response

The rate-dependent, viscoelastic material response is accounted for by four nonlinear, Maxwell-like, non-equilibrium mechanisms in parallel with the equilibrium response (Fig. 1.1). For each non-equilibrium branch, denoted by the index α, the deformation gradient $\mathbf{F}$ is multiplicatively decomposed into elastic and viscous parts: $\mathbf{F} = \mathbf{F}^{\mathrm{e}(\alpha)}\mathbf{F}^{\mathrm{v}(\alpha)}$, where $\mathbf{F}^{\mathrm{e}(\alpha)}$ is the non-equilibrium elastic distortion, representing the deformation of "spring" α, with $J^{\mathrm{e}(\alpha)} = \det \mathbf{F}^{\mathrm{e}(\alpha)} > 0$, and $\mathbf{F}^{\mathrm{v}(\alpha)}$ is the viscous distortion, representing the deformation of "dashpot" α, with $J^{\mathrm{v}(\alpha)} = \det \mathbf{F}^{\mathrm{v}(\alpha)} > 0$.

The free energy due to the elastic distortion of each non-equilibrium mechanism $\psi_{\mathrm{neq}}^{(\alpha)}$ is based on the elastic logarithmic strain tensor $\mathbf{E}^{\mathrm{e}(\alpha)}$, utilizing the following definitions: $\mathbf{F}^{\mathrm{e}(\alpha)} = \mathbf{V}^{\mathrm{e}(\alpha)}\mathbf{R}^{\mathrm{e}(\alpha)}$, left polar decomposition of $\mathbf{F}^{\mathrm{e}(\alpha)}$; $\mathbf{V}^{\mathrm{e}(\alpha)} = \sum_{i=1}^{3}(\lambda_i^{\mathrm{e}(\alpha)})\mathbf{l}_i^{\mathrm{e}(\alpha)} \otimes \mathbf{l}_i^{\mathrm{e}(\alpha)}$, spectral decomposition of $\mathbf{V}^{\mathrm{e}(\alpha)}$; $\mathbf{E}^{\mathrm{e}(\alpha)} = \sum_{i=1}^{3}(\ln \lambda_i^{\mathrm{e}(\alpha)})\mathbf{l}_i^{\mathrm{e}(\alpha)} \otimes \mathbf{l}_i^{\mathrm{e}(\alpha)}$, elastic logarithmic strain tensor; $K_1^{\mathrm{e}(\alpha)} = \mathrm{tr}\,(\mathbf{E}^{\mathrm{e}(\alpha)})$, elastic dilatation; $K_2^{\mathrm{e}(\alpha)} = |\mathrm{dev}\,(\mathbf{E}^{\mathrm{e}(\alpha)})|$, magnitude of elastic distortion; and $K_3^{\mathrm{e}(\alpha)} = 3\sqrt{6}\det(\mathrm{dev}\,(\mathbf{E}^{\mathrm{e}(\alpha)})/K_2^{\mathrm{e}(\alpha)})$, mode of elastic distortion. The constitutive response of each non-equilibrium "spring" in Figure 1.1 is described by a non-equilibrium free energy function $\tilde{\psi}_{\mathrm{neq}}^{(\alpha)}(K_1^{\mathrm{e}(\alpha)}, K_2^{\mathrm{e}(\alpha)}, K_3^{\mathrm{e}(\alpha)})$, and the corresponding non-equilibrium contribution to the Cauchy stress for each mechanism α is then given through the derivatives of the non-equilibrium free energy function by

$$\mathbf{T}_{\mathrm{neq}}^{(\alpha)} = J^{\mathrm{e}(\alpha)-1}\left[\frac{\partial\tilde{\psi}_{\mathrm{neq}}^{(\alpha)}}{\partial K_1^{\mathrm{e}(\alpha)}}\mathbf{1} + \frac{\partial\tilde{\psi}_{\mathrm{neq}}^{(\alpha)}}{\partial K_2^{\mathrm{e}(\alpha)}}\mathbf{N}^{\mathrm{e}(\alpha)} + \frac{\partial\tilde{\psi}_{\mathrm{neq}}^{(\alpha)}}{\partial K_3^{\mathrm{e}(\alpha)}}\frac{1}{K_2^{\mathrm{e}(\alpha)}}\mathbf{Y}^{\mathrm{e}(\alpha)}\right], \tag{1.6}$$

where $\mathbf{N}^{\mathrm{e}(\alpha)} = \mathrm{dev}\,(\mathbf{E}^{\mathrm{e}(\alpha)})/K_2^{\mathrm{e}(\alpha)}$ and $\mathbf{Y}^{\mathrm{e}(\alpha)} = 3\sqrt{6}\mathbf{N}^{\mathrm{e}(\alpha)^2} - \sqrt{6}\mathbf{1} - 3K_3^{\mathrm{e}(\alpha)}\mathbf{N}^{\mathrm{e}(\alpha)}$. The total Cauchy stress is then given by $\mathbf{T} = \mathbf{T}_{\mathrm{eq}} + \sum_{\alpha=1}^{4}\mathbf{T}_{\mathrm{neq}}^{(\alpha)}$ [36].

Following the decomposition of the equilibrium free-energy function (1.2), we take the constitutive equation for the non-equilibrium free-energy function $\tilde{\psi}_{\mathrm{neq}}^{(\alpha)}(K_1^{\mathrm{e}(\alpha)}, K_2^{\mathrm{e}(\alpha)}, K_3^{\mathrm{e}(\alpha)})$ for each mechanism α to be additively decomposed as follows:

$$\begin{aligned}\tilde{\psi}_{\mathrm{neq}}^{(\alpha)}(K_1^{\mathrm{e}(\alpha)}, K_2^{\mathrm{e}(\alpha)}, K_3^{\mathrm{e}(\alpha)}) = G_{\mathrm{neq}}^{(\alpha)}\left[X_{\mathrm{neq}}^{(\alpha)}(K_1^{\mathrm{e}(\alpha)})(K_2^{\mathrm{e}(\alpha)})^2 + L_{\mathrm{neq}}^{(\alpha)}(K_2^{\mathrm{e}(\alpha)}, K_3^{\mathrm{e}(\alpha)})\right]\\ + B_{\mathrm{neq}}^{(\alpha)} f_{\mathrm{neq}}^{(\alpha)}(K_1^{\mathrm{e}(\alpha)}),\end{aligned} \tag{1.7}$$

where $G_{\mathrm{neq}}^{(\alpha)}$ and $B_{\mathrm{neq}}^{(\alpha)}$ are the ground-state shear and bulk moduli, respectively, for each mechanism α, and $X_{\mathrm{neq}}^{(\alpha)}(K_1^{\mathrm{e}(\alpha)})$, $L_{\mathrm{neq}}^{(\alpha)}(K_2^{\mathrm{e}(\alpha)}, K_3^{\mathrm{e}(\alpha)})$, and $f_{\mathrm{neq}}^{(\alpha)}(K_1^{\mathrm{e}(\alpha)})$ are phenomenological fitting functions for each mechanism α.

For the non-equilibrium branches, we use the same functional forms for $X_{\mathrm{neq}}^{(\alpha)}$, $L_{\mathrm{neq}}^{(\alpha)}$, and $f_{\mathrm{neq}}^{(\alpha)}$ in (1.7) that we do for X_{eq}, L_{eq}, and f_{eq} of the equilibrium branch. For simplicity, the parameters in $X_{\mathrm{neq}}^{(\alpha)}$ and $f_{\mathrm{neq}}^{(\alpha)}$, $\{K_1^0, \Delta_{\mathrm{K}}, X_1', X_2', C_2, C_3, r, J_{\min}\}$, are constrained to be the same as the parameters appearing in X_{eq} and f_{eq}. To further reduce the model complexity, the ratio of the non-equilibrium bulk and shear moduli for each branch $B_{\mathrm{neq}}^{(\alpha)}/G_{\mathrm{neq}}^{(\alpha)} = B/G_0$ is constrained to be equal across all non-equilibrium branches and equal to the ratio for the equilibrium response. Finally, to accommodate experimental data in simple tension, the higher-order distortional response is allowed to have branch-dependent parameters $C_{1\mathrm{neq}}^{(\alpha)}$ and $q_{\mathrm{neq}}^{(\alpha)}$, while the parameters C_0 and p are constrained to be the same as those appearing in (1.4) for all branches.

The evolution of the viscous distortion $\mathbf{F}^{\mathrm{v}(\alpha)}$ for each non-equilibrium mechanism α (which describes the constitutive response of each "dashpot" in Figure 1.1) is given by

$$\dot{\mathbf{F}}^{\mathrm{v}(\alpha)} = \mathbf{D}^{\mathrm{v}(\alpha)}\mathbf{F}^{\mathrm{v}(\alpha)}, \quad \mathbf{F}^{\mathrm{v}(\alpha)}(\mathbf{X}, t=0) = \mathbf{1}, \tag{1.8}$$

where $\mathbf{D}^{\mathrm{v}(\alpha)}$ is the symmetric viscous stretching tensor. The constitutive equation for the viscous stretching for each mechanism α is given through the Mandel stress for that mechanism $\mathbf{M}^{\mathrm{e}(\alpha)}$, which, for an isotropic material, is related to the non-equilibrium Cauchy stress for each mechanism $\mathbf{T}_{\mathrm{neq}}^{(\alpha)}$ through

$$\mathbf{M}^{\mathrm{e}(\alpha)} = J^{\mathrm{e}(\alpha)}\mathbf{R}^{\mathrm{e}(\alpha)\top}\mathbf{T}_{\mathrm{neq}}^{(\alpha)}\mathbf{R}^{\mathrm{e}(\alpha)}. \tag{1.9}$$

We define the equivalent shear stress for each mechanism α as

$$\bar{\tau}^{(\alpha)} = \sqrt{\operatorname{dev}(\mathbf{M}^{\mathrm{e}(\alpha)}) : \operatorname{dev}(\mathbf{M}^{\mathrm{e}(\alpha)})/2} \tag{1.10}$$

and adopt the following constitutive equation for $\mathbf{D}^{\mathrm{v}(\alpha)}$:

$$\begin{cases} \mathbf{D}^{\mathrm{v}(\alpha)} = \dot{\bar{\gamma}}^{\mathrm{v}(\alpha)} \dfrac{\operatorname{dev}(\mathbf{M}^{\mathrm{e}(\alpha)})}{2\bar{\tau}^{(\alpha)}} + \dfrac{1}{3}\dot{\varepsilon}^{\mathrm{v}(\alpha)} \operatorname{sign}\left(\operatorname{tr}(\mathbf{M}^{\mathrm{e}(\alpha)})\right)\mathbf{1}, \\ \dot{\bar{\gamma}}^{\mathrm{v}(\alpha)} = \dot{\gamma}_0^{(\alpha)} \left(\dfrac{\bar{\tau}^{(\alpha)}}{\tau_0^{(\alpha)}}\right)^{\frac{1}{m^{(\alpha)}}}, \\ \dot{\varepsilon}^{\mathrm{v}(\alpha)} = \dot{\varepsilon}_0^{(\alpha)} \left(\dfrac{|\operatorname{tr}(\mathbf{M}^{\mathrm{e}(\alpha)})|}{3\sigma_0^{(\alpha)}}\right)^{\frac{1}{m^{(\alpha)}}}, \end{cases} \tag{1.11}$$

where $\dot{\bar{\gamma}}^{\mathrm{v}(\alpha)}$ and $\dot{\varepsilon}^{\mathrm{v}(\alpha)}$ are functions of Mandel stress invariants and denote the equivalent shear viscous strain rate and the volumetric viscous strain rate, respectively. The material parameter $0 < m^{(\alpha)} \leq 1$ represents a strain-rate sensitivity exponent for mechanism α, which is taken to be the same for both the equivalent shear $(1.11)_2$ and volumetric $(1.11)_3$ parts of the viscous response. The parameter $\dot{\gamma}_0^{(\alpha)} > 0$ is a reference shear strain rate; $\dot{\varepsilon}_0^{(\alpha)} > 0$ is a reference volumetric strain rate; $\tau_0^{(\alpha)} > 0$ is a reference shear stress; and $\sigma_0^{(\alpha)} > 0$ is a reference mean stress. Only one of $\dot{\gamma}_0^{(\alpha)}$ and $\tau_0^{(\alpha)}$ is an independent fitting parameter for the deviatoric response, and similarly, only one of $\dot{\varepsilon}_0^{(\alpha)}$ and $\sigma_0^{(\alpha)}$ is an independent fitting parameter for the volumetric response.

Let $\eta^{(\alpha)} = \bar{\tau}^{(\alpha)}/\dot{\bar{\gamma}}^{\mathrm{v}(\alpha)}$ and $\kappa^{(\alpha)} = |\mathrm{tr}\,(\mathbf{M}^{\mathrm{e}(\alpha)})|/3\dot{\varepsilon}^{\mathrm{v}(\alpha)}$ denote the shear and bulk viscosities for non-equilibrium mechanism α, respectively, which are in general non-Newtonian viscosities that depend on the respective viscous strain rates $\dot{\bar{\gamma}}^{\mathrm{v}(\alpha)}$ and $\dot{\varepsilon}^{\mathrm{v}(\alpha)}$. If $m^{(\alpha)} = 1$, the non-equilibrium mechanism α reduces to a Newtonian branch, and if $m^{(\alpha)} < 1$, the mechanism α is a shear thinning branch. To reduce model complexity and the number of adjustable material parameters, only one non-equilibrium branch ($\alpha = 1$) is a shear thinning branch, while three non-equilibrium branches ($\alpha = 2,3,4$) are Newtonian branches. For all three Newtonian branches, since $m^{(\alpha)} = 1$, the shear viscosity $\eta^{(\alpha)} = \bar{\tau}^{\alpha}/\dot{\bar{\gamma}}^{\mathrm{v}(\alpha)}$ and the bulk viscosity $\kappa^{(\alpha)} = |\mathrm{tr}\,(\mathbf{M}^{\mathrm{e}(\alpha)})|/3\dot{\varepsilon}^{\mathrm{v}(\alpha)}$ are constants. The number of parameters is further reduced by taking the shear and bulk viscosities to be equal, i.e., $\eta^{(\alpha)} = \kappa^{(\alpha)}$, for each branch. Therefore, denoting the shear relaxation time as $t_0^{(\alpha)} = \eta^{(\alpha)}/G_{\mathrm{neq}}^{(\alpha)}$, for each Newtonian branch, there are two additional material parameters: $\{G_{\mathrm{neq}}^{(\alpha)}, t_0^{(\alpha)}\}$ with $\{B_{\mathrm{neq}}^{(\alpha)}, \eta^{(\alpha)}, \kappa^{(\alpha)}\}$ then given through $B_{\mathrm{neq}}^{(\alpha)} = (B_0/G_0)G_{\mathrm{neq}}^{(\alpha)}$, $\eta^{(\alpha)} = G_{\mathrm{neq}}^{(\alpha)}t_0^{(\alpha)}$, and $\kappa^{(\alpha)} = \eta^{(\alpha)}$, respectively. Similarly, for the shear thinning branch, the number of parameters is reduced by taking $\tau_0^{(\alpha)} = \sigma_0^{(\alpha)}$. Because $\dot{\gamma}_0^{(\alpha)}$ is not an independent fitting parameter distinct from $\tau_0^{(\alpha)}$, we fix $\tau_0^{(\alpha)} = \sigma_0^{(\alpha)} = 100\,\mathrm{kPa}$. To further reduce model complexity, we constrain $\dot{\varepsilon}_0^{(\alpha)} = \dot{\gamma}_0^{(\alpha)}$. Therefore, for the shear thinning branch there are three additional fitting parameters: $\{G_{\mathrm{neq}}^{(\alpha)}$, $m^{(\alpha)}$, $\dot{\gamma}_0^{(\alpha)}\}$. Table 1.2 summarizes the non-equilibrium parameters for the closed-cell EVA

Non-equilibrium material parameters								
$G_{\text{neq}}^{(1)}$ [kPa]	$m^{(1)}$	$\dot{\gamma}_0^{(1)}$ [s^{-1}]	$C_{1\text{neq}}^{(1)}$	$q_{\text{neq}}^{(1)}$	$G_{\text{neq}}^{(2)}$ [kPa]	$t_0^{(2)}$ [s]	$C_{1\text{neq}}^{(2)}$	$q_{\text{neq}}^{(2)}$
580	0.18	3500	0	/	90	50	0	/
$G_{\text{neq}}^{(3)}$ [kPa]	$t_0^{(3)}$ [s]	$C_{1\text{neq}}^{(3)}$	$q_{\text{neq}}^{(3)}$		$G_{\text{neq}}^{(4)}$ [kPa]	$t_0^{(4)}$ [s]	$C_{1\text{neq}}^{(4)}$	$q_{\text{neq}}^{(4)}$
80	2	2.5	2.1		50	0.1	0	/

Table 1.2: Non-equilibrium material parameters for the closed-cell EVA foam, reported in Li et al. [34].

foam. These parameters were estimated using simple compression/tension data over the strain-rate range from 10^{-3} s^{-1} to 10^{1} s^{-1} in Li et al. [34], and interested readers are referred to Figures 2 and 3 of Li et al. [34] to see the fitted stress/strain curves.

1.3 Thesis Contributions

The purpose of this thesis is twofold:

1. to elucidate the role of selected material properties in the constitutive model of Section 1.2 through parametric studies in which these material properties are varied in finite-element simulations of cyclic indentation and

2. to apply this constitutive model for EVA foam to simulations of cyclic loading of a shoe midsole.

The effect of each parametric study was quantified through the maximum force applied and the dissipation efficiency of the foam (defined in Chapter 2).

The remainder of this thesis is organized as follows. In Chapter 2, we describe how both equilibrium and non-equilibrium properties of the constitutive model affect the response of a foam substrate, utilizing an axisymmetric finite-element model. Then, in Chapter 3, we apply the constitutive model to a shoe midsole and examine the effects of the loading frequency and the position of a flat, circular indenter on the foam model. Lastly, we close with concluding remarks and future directions in Chapter 4.

Chapter 2

The Effects of Material Parameters: Parametric Studies in Cyclic Indentation

The first part of this study focused on the roles of various material parameters appearing in the constitutive model of Section 1.2. To elucidate the effect of each parameter under consideration on the predicted material response, we carried out parametric studies for both equilibrium (Section 2.2) and non-equilibrium (Section 2.3) properties. These studies were performed using Abaqus simulations, in which a flat, circular indenter is cyclically pressed into a layer of foam (Section 2.1). The effect of each parametric study was quantified through the maximum force applied and the dissipation efficiency of the foam.

2.1 Simulation Details and Baseline Results

The geometric configuration for the finite-element simulations was based on internal testing procedures at Reebok International Ltd (the so-called Dynamic Impact Test (DIT)) with experimental specifications as follows:

- Force control,
- 1000 indentation cycles at a loading frequency of 3 Hz,

- Target force = 500 N (i.e., target pressure of 323 kPa),
- Indenter geometry: flat, circular contact surface with an area of 15.548 cm^2
- Foam geometry: 14-16 mm thick sheet, 10 cm long $\times$ 10 cm wide

As shown in Figure 2.1, a simplified representation of Reebok's experimental procedure was adapted for use in the numerical simulations of the present work. An axisymmetric model was utilized, idealizing both the indenter and the foam substrate to be circular in cross-section. The radius of the indenter (r_i) was $\sqrt{15.548/\pi}$ cm to reproduce the same contact area as in experimental testing, and its height (h) was 2 cm. The corners of the indenter were rounded with a radius (r_c) of 0.5 mm to ensure a smoother contact area with the foam and to mitigate potential numerical issues. The radius of the foam substrate (R_0) was 10 cm with a thickness (H) of 15 mm. The foam substrate was meshed using 9,690 Abaqus-CAX4R elements (four-node, axisymmetric, quadrilateral, reduced-integration elements with hourglass control) and the indenter was idealized as a rigid surface. Contact between the foam substrate and the indenter was idealized with a friction coefficient of 0.4 in the simulations.

Regarding boundary conditions, nodes along the bottom of the foam substrate were

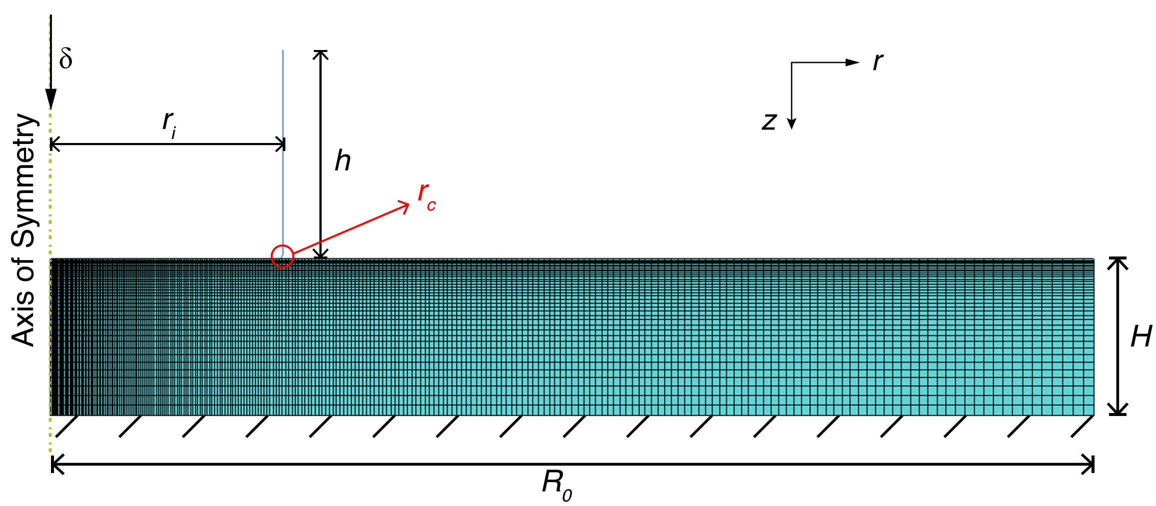

Figure 2.1: Finite-element configuration for axisymmetric numerical simulations of cyclic indentation of a foam substrate.

bounded in both directions ($u_r = u_z = 0$), and the nodes along the left side (on the axis of symmetry) were bounded in the r direction. The displacement (δ) of the indenter was prescribed at its reference point, in which the only non-zero displacement component allowed was along the z direction. This motion was prescribed so that the indenter completed three cycles of loading onto and unloading off of the foam substrate, imposing uniaxial compression-like deformation in the foam material beneath the indenter. Four different loading frequencies of this cyclic motion were considered: 3 Hz, 0.3 Hz, 0.03 Hz, and 0.003 Hz.

All finite-element calculations were performed in Abaqus/Explicit, using the user-material (VUMAT) subroutine implementation of the constitutive model in Section 1.2 developed in Li et al. [34]. The primary data collected in each simulation was the reaction force history experienced by the indenter during cyclic indentation on the foam. This information allowed for the creation of plots of indenter force versus displacement and for the quantification of the force-level experienced by the indenter as well as the hysteresis the foam material undergoes. Since foam materials, such as EVA, are used for their energy dissipation capacity, we define a dissipation efficiency as the ratio of the area between the loading and unloading curves to the entire area under the loading curve. A visual representation of the indenter force versus displacement history is shown in Figure 2.2 for a baseline case with the material parameters given in Section 1.2 and a loading frequency of 3 Hz. After one cycle, a stabilized hysteresis loop was attained, and the loading and unloading curves are labeled in Figure 2.2.

Although the Reebok testing protocol uses force (load) control, the representative simulation results in Figure 2.2 were obtained under displacement control. To establish that the dissipation efficiency may be characterized under either force or displacement control, simulations were performed using both protocols. For load control, the force applied to the indenter was cycled between 10 N to 500 N with a sinusoidal force history. Note that in an explicit finite-element simulation under load control, the mass of the indenter must be

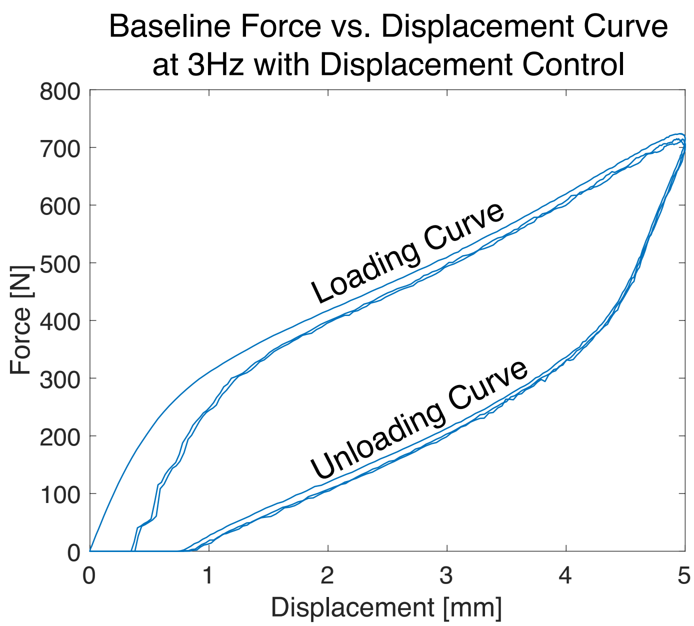

Figure 2.2: Baseline force versus displacement curve for EVA foam under cyclic indentation at 3 Hz with displacement control.

prescribed, so a density was also prescribed to the indenter in load control. All numerical simulations were performed under quasi-static conditions, so the value of the density does not affect the reported results, but for specificity, aluminum was the material choice with a density of 2,710 kg/m^3. For displacement control, the indenter displacement cycled between 0 mm to 5 mm pressing into the foam with a sinusoidal displacement history. Figure 2.3 shows that when comparing the calculated dissipation efficiencies for both displacement and load control as a function of loading frequency, there is no significant difference between the two types of protocols. As a result, all subsequent simulations were completed using displacement control as this control is more manageable and straightforward to apply in numerical simulations.

2.2 Equilibrium Material Parameters

The material parameters appearing in the equilibrium response of the large-deformation, viscoelastic constitutive model are listed in Table 1.1 along with the baseline values for EVA.

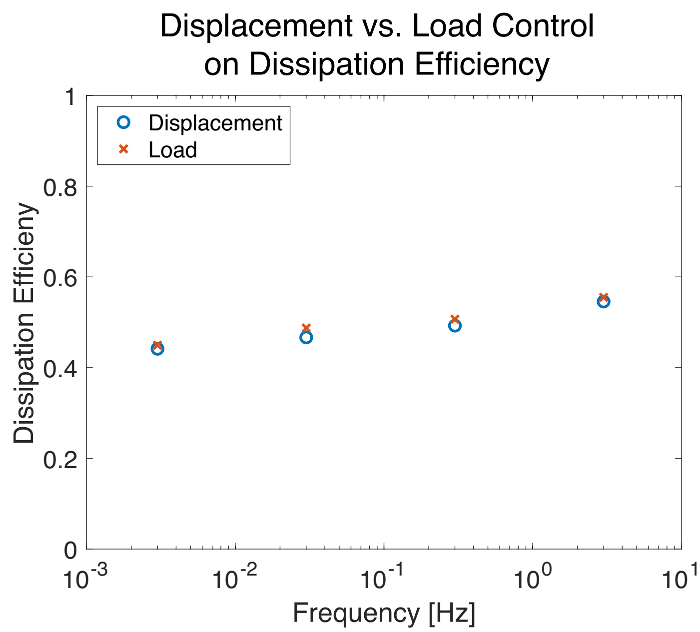

Figure 2.3: Comparison of calculated dissipation efficiency under displacement and load control during cyclic indentation.

In our parametric studies, the equilibrium parameters of interest are the ground-state shear modulus (G_0), the ground-state bulk modulus (B), and the volumetric locking value (J_{min}).

2.2.1 Shear and Bulk Moduli

The ground-state shear (G_0) and bulk (B) moduli were changed by the same factor for each case in this parametric study, so that the ratio (G_0/B) was kept constant. The baseline values for G_0 and B were 500 kPa and 1000 kPa, respectively, and were multiplied by 10, 50, and 100 at each frequency. Figure 2.4 displays the effect of varying these two moduli on the force versus displacement curves. A notable difference between the curves at each frequency is that the maximum force experienced by the foam was increased as the moduli increased. This is illustrated in Figure 2.5(left), which shows that the peak force increases with the moduli values and that at the highest value of G_0 and B, the peak force is nearly frequency-independent. Also, compared to Figure 2.3, the hysteresis loop is not visible, indicating that as the magnitude of G_0 and B increased, the path of loading and unloading

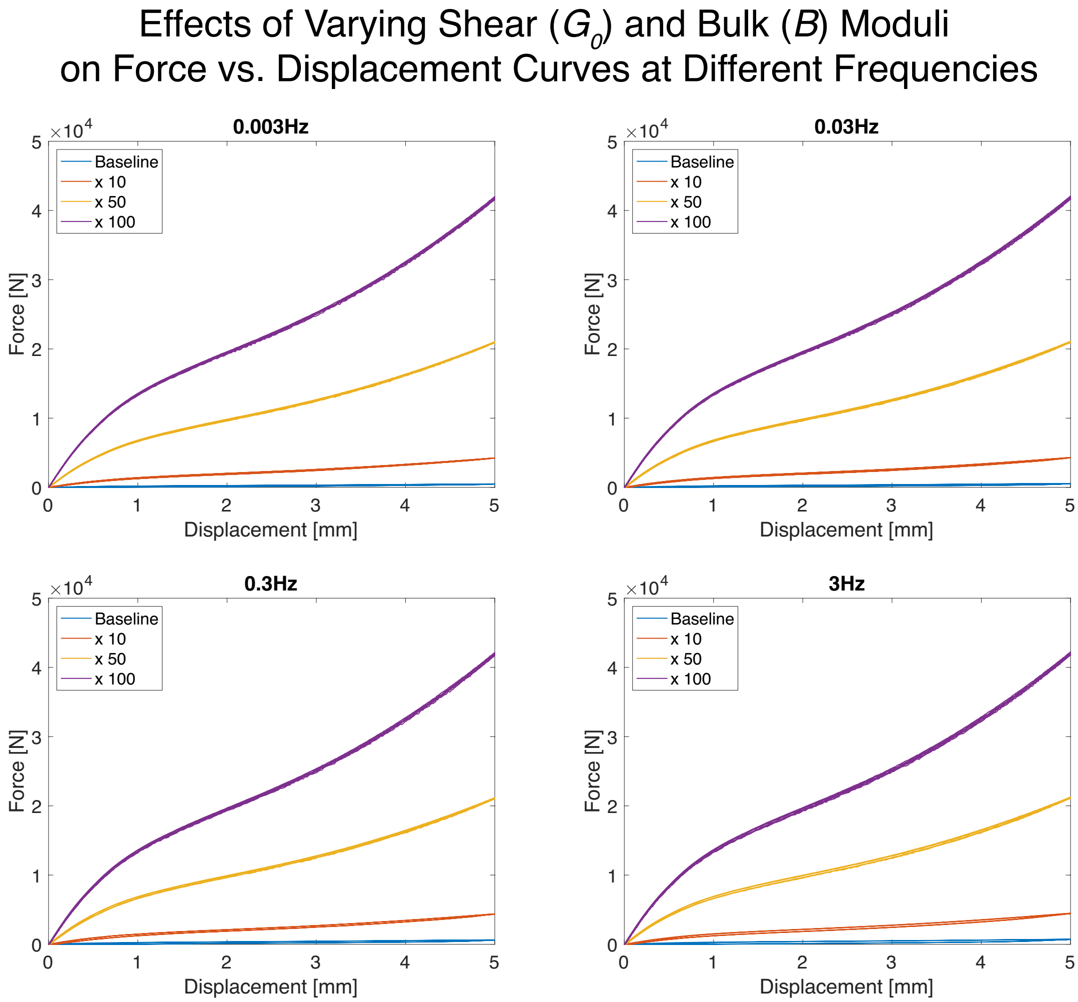

Figure 2.4: Force versus displacement curves during cyclic indentation when varying frequency and the ground-state moduli, G_0 and B.

of the indenter in terms of force became nearly the same. This is explicitly shown through Figure 2.5(right), where the dissipation efficiency decreases as the moduli values increase and at the highest value of G_0 and B, the dissipation efficiency is almost zero across all four frequencies.

The results of this parametric study agree with the notion of the material moduli. By increasing G_0 and B, the material responds in a stiffer manner, resulting in more force being applied in order to deform the material to the same amount. Moreover, in this parametric study, only the equilibrium moduli are increased with the non-equilibrium moduli remaining

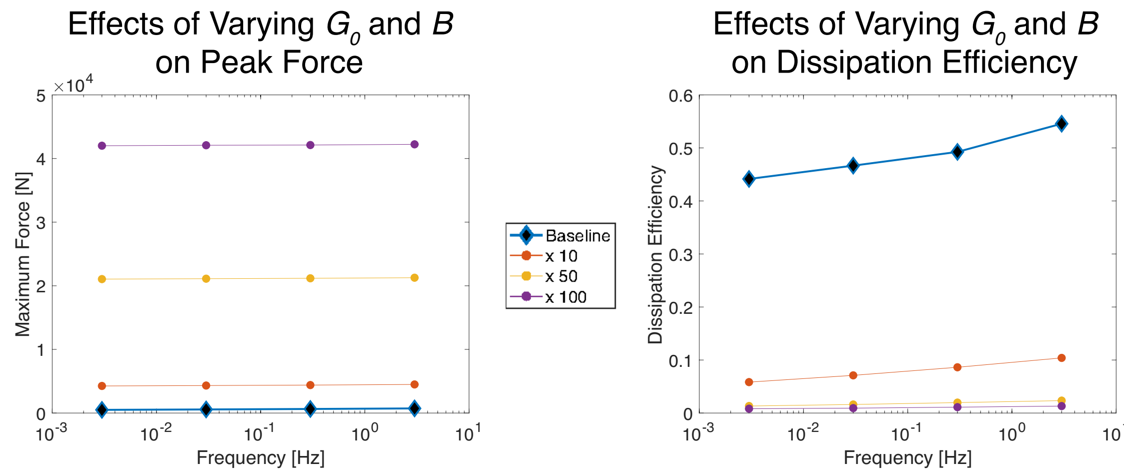

Figure 2.5: Peak forces and dissipation efficiencies as a function of frequency during cyclic indentation when varying G_0 and B.

fixed. Therefore, the material responds in a more elastic manner, while the capacity of the material to dissipate energy per cycle does not increase, resulting in a decreased dissipation efficiency.

2.2.2 Volumetric Locking

As introduced in Section 1.2.1, the volumetric locking parameter (J_{min}) quantifies the minimum allowable value of volume ratio (J). A physical interpretation of this parameter is through the porosity (volume fraction of air) of the undeformed material (ϕ), where the volumetric locking parameter may be interpreted as $J_{min} = 1 - \phi$. Increasing J_{min} (i.e., decreasing ϕ) results in the material becoming stiffer sooner as there is less air in the material to squeeze out. The baseline value of J_{min} was 0.16 (Table 1.1), and for the parametric studies, values of 0.1, 0.2, and 0.25 were considered.

Figure 2.6 displays the effect of varying J_{min} on the force versus displacement curves. Similar to the effect of increasing G_0 and B, a material with higher J_{min} generated a higher force to reach the same amount of displacement. However, note from Figure 2.6 that the force increase is only observed at high displacements and that the initial slope of the force versus displacement curves is unaffected by J_{min}. Unlike G_0 and B, which increase the

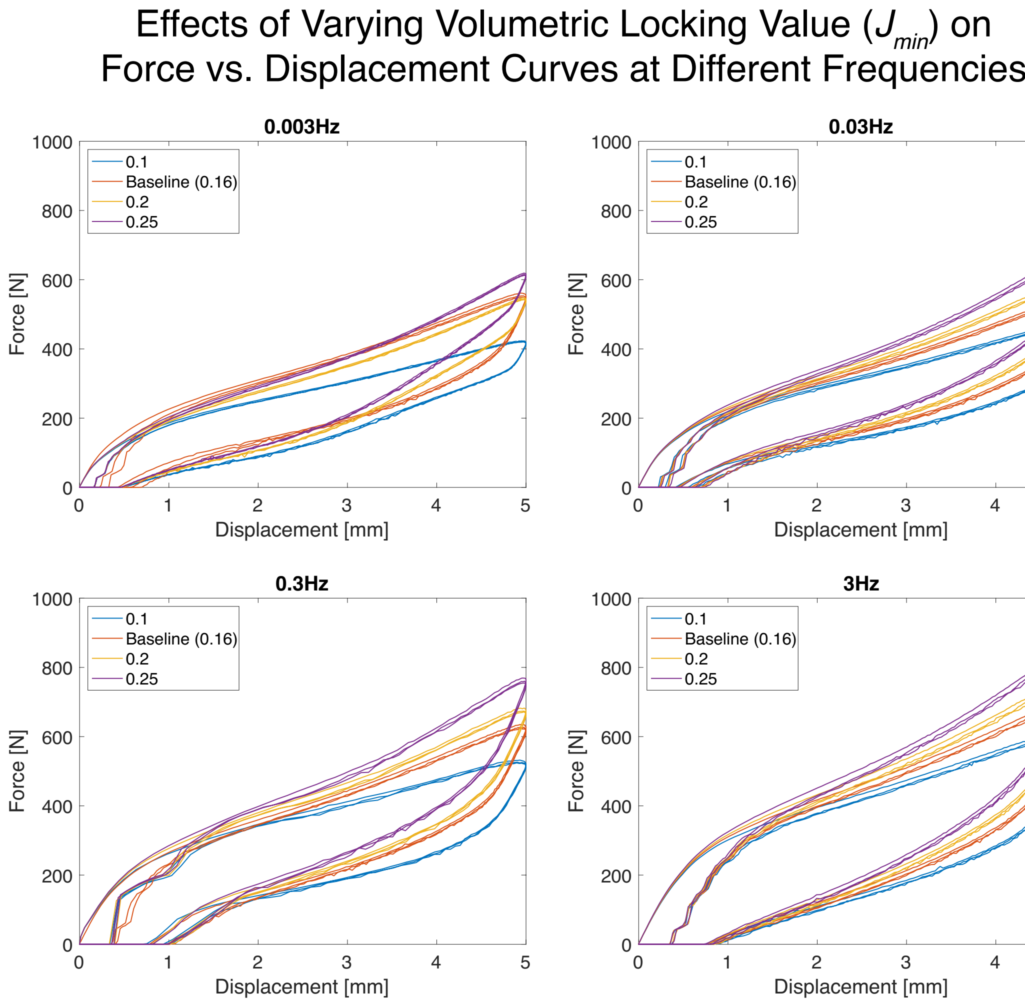

Figure 2.6: Force versus displacement curves during cyclic indentation when varying frequency and the volumetric locking parameter, J_{min}.

entire force versus displacement curves, the locking parameter J_{min} only affects the large deformation response. As a result, the change in force for the J_{min} parametric study was not as drastic as for G_0 and B, and the hysteresis loops are still visible. Thus, the material remains able to dissipate a discernible amount of energy for all J_{min} values tested.

Figure 2.7 explicitly shows how the peak forces and dissipation efficiencies varied with frequency and the value of the volumetric locking parameter J_{min}. With a J_{min} value of 0.1, the peak forces were the lowest, however the dissipation efficiencies were the highest. Thus, increasing J_{min} increased the peak force and resulted in a decrease of dissipation efficiency at each frequency. In fact, we note that within the range of J_{min} considered, increasing the value

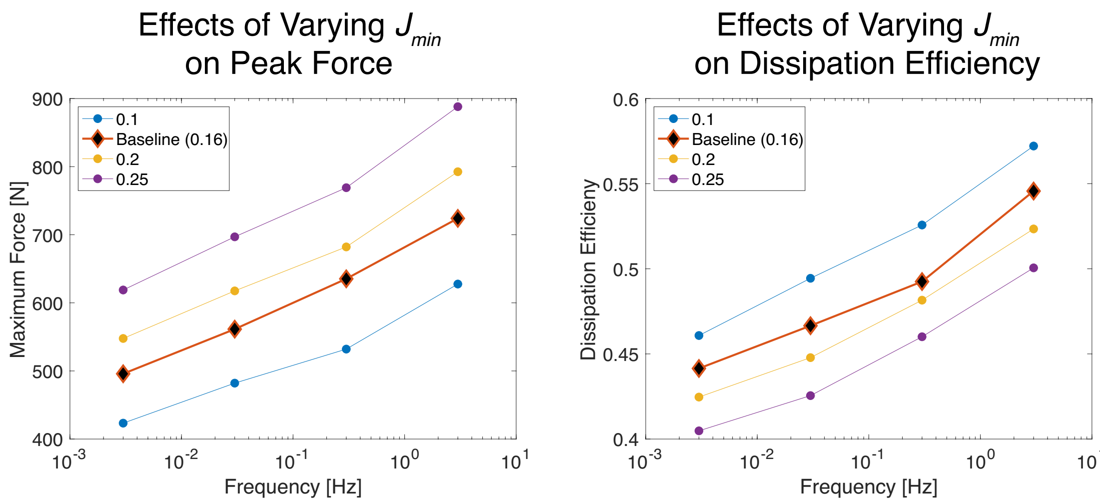

Figure 2.7: Peak forces and dissipation efficiencies as a function of frequency during cyclic indentation when varying J_{min}.

of J_{min} leads to an approximate upward shift of the peak force curve and an approximate downward shift of the dissipation efficiency curve in Figure 2.7. Moreover, the dissipation efficiency depends nearly linearly on J_{min} for all frequencies. For example, a change of ± 0.05 for J_{min} resulted in a change of approximately ∓ 0.02 for the dissipation efficiency.

2.3 Non-Equilibrium Material Parameters

Next, we consider the effects of several non-equilibrium material parameters. The non-equilibrium shear moduli for each of the non-equilibrium branches ($G_{neq}^{(\alpha)}$) were the main parameters of interest. As explained in Section 1.2, there are four non-equilibrium branches in the constitutive model, of which the first non-equilibrium branch (Branch 1) behaves differently than the other three branches (Branch 2, Branch 3, and Branch 4). More specifically, Branch 1 is a non-Newtonian, shear-thinning branch, while Branches 2, 3, and 4 are Newtonian branches. As a result, Branch 1 involves an additional material parameter, the strain-rate sensitivity exponent ($m^{(1)}$), and an additional parametric study for this material parameter was carried out for this branch.

2.3.1 Branch 1

Strain-Rate Sensitivity Exponent and Correlating Reference Shear Strain Rate

The baseline strain-rate sensitivity exponent ($m^{(1)}$) was 0.18 and the correlating reference shear strain rate ($\dot{\gamma}_0^{(1)}$) was 3500 s^{-1} (Table 1.2). For brevity, throughout the remainder of this section, we drop the superscripts and refer to these material parameters as m and $\dot{\gamma}_0$. For the parametric study, the value of m was changed to 0.1, 0.15, 0.2, and 0.25. For each case of m, the value of $\dot{\gamma}_0$ was also changed so that the equivalent shear stress ($\bar{\tau}$) would be the same at a reference equivalent shear viscous strain rate of $\dot{\bar{\gamma}}^{\mathrm{v}} = 10^{-3}\,\mathrm{s}^{-1}$ (Equation 1.11_2). Denote the baseline values of m and $\dot{\gamma}_0$ as $m^* = 0.18$ and $\dot{\gamma}_0^* = 3500\,\mathrm{s}^{-1}$, respectively. Based on Equation 1.11, Equation 2.1 gives how the new values of $\dot{\gamma}_0$ were calculated using each of the values of m under consideration:

$$\dot{\gamma}_0 = (10^{-3}\,\mathrm{s}^{-1})\left(\frac{\dot{\gamma}_0^*}{10^{-3}\,\mathrm{s}^{-1}}\right)^{m^*/m}. \tag{2.1}$$

Calculating $\dot{\gamma}_0$ in this way for each new value of m ensures that the response of the foam material in cyclic indentation at low loading frequency is nearly the same for all values of m under consideration and that the effect of varying m will be most evident at the higher loading frequencies. Table 2.1 summarizes the correlating values of $\dot{\gamma}_0$ for each of the values of m under consideration.

Figure 2.8 displays the effect of varying m on the force versus displacement curves for all four frequencies. For the lowest frequency (0.003 Hz), there is little difference between the curves for the different values of m. This lack of dependence on m for the lowest frequency is also demonstrated in Figure 2.9(left) as the maximum forces have approximately the same value for the lowest frequency for all values of m. This is due to the fact that the

m	0.1	0.15	0.18	0.2	0.25
$\dot{\gamma}_0$ [s^{-1}]	6.016×10^8	7.127×10^4	3.500×10^3	7.756×10^2	5.149×10^1

Table 2.1: Values of m and correlating values of $\dot{\gamma}_0$

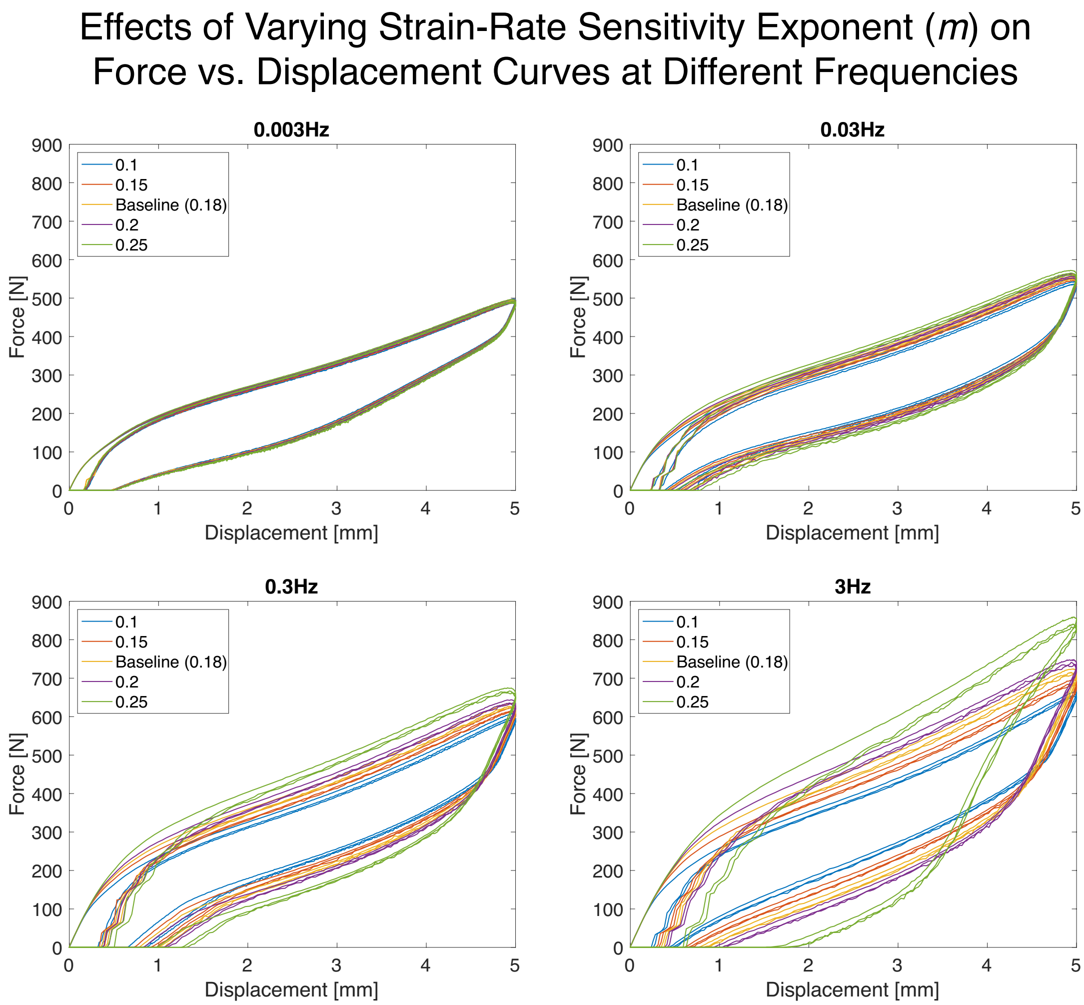

Figure 2.8: Force versus displacement curves during cyclic indentation when varying m.

reference strain rate $\dot{\gamma}_0$ was constrained using Equation 2.1 where $10^{-3}\ \mathrm{s}^{-1}$ was the target equivalent shear viscous strain rate. As the frequency increases, differences between the force versus displacement curves for different values of m become evident in Figure 2.8, and the dependence of the peak force on frequency in Figure 2.9(left) becomes different for the different values of m.

In Figure 2.9(left), the peak force increases more rapidly with frequency as the value of m is increased. Recall that Branch 1 is a non-Newtonian, shear-thinning branch and is therefore less rate-dependent than the other non-equilibrium branches. At the lowest value of m considered in this study (0.1), the dependence of the peak force on frequency

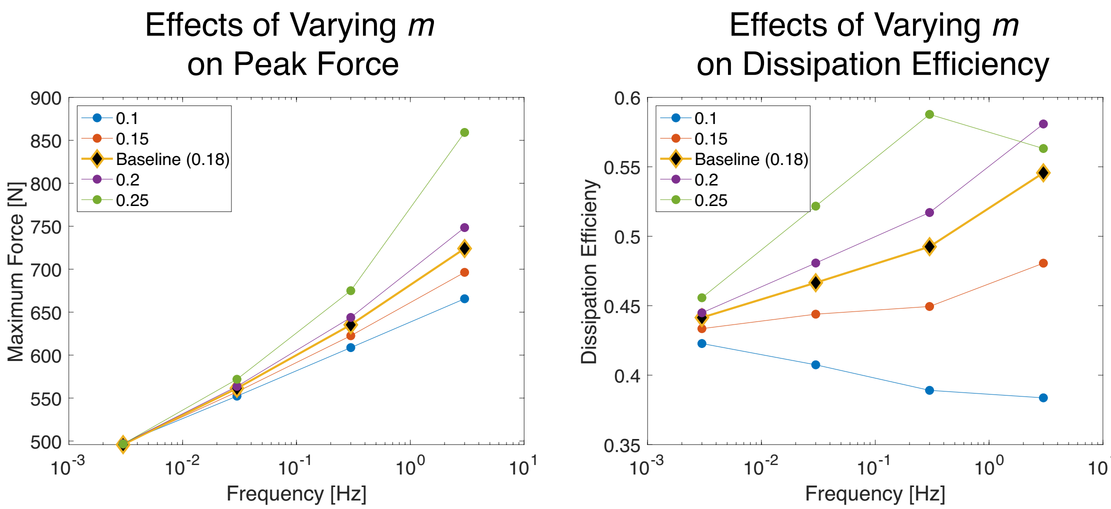

Figure 2.9: Peak forces and dissipation efficiencies as a function of frequency during cyclic indentation when varying m.

is the weakest, while as m increases, Branch 1 becomes more rate-dependent, in which increasing the frequency leads to a strong increase in the peak force. Once m is increased to the maximum value considered in this study (0.25), there is a steep increase in peak force as the frequency is increased from 0.3 Hz to 3 Hz, indicating that for $m = 0.25$ and loading frequencies on the order of 10^0-10^1 s^{-1}, Branch 1 will have a strong impact on the rate-dependence of the material behavior.

The dissipation efficiency also has similar trends as the peak force, in which the values are closer at the lowest frequency then start to separate as the frequency increases. An interesting result arises when m has the value of 0.1. In this case, the dissipation efficiency decreases as the frequency increases, which is opposite to the other values of m (with an exception of when m is 0.25 and the frequency increases from 0.3 Hz to 3 Hz). This difference for the case of $m = 0.1$ is likely due to the fact that Branch 1 is less rate-dependent when m is sufficiently small. Thus, Branch 1's contribution to the material's hysteresis remains nearly constant as the frequency increases for this value of m, while the peak force continues to increase, leading to a decrease in the dissipation efficiency. However, when m was 0.15 and above, a higher maximum force was accompanied by sufficiently large increase in the amount of hysteresis, yielding a higher dissipation efficiency with increasing frequency (again, with the exception of when m is 0.25 and the frequency increases from 0.3Hz to 3Hz). Therefore, increasing m allows for Branch 1 to have a greater impact on the rate-dependent material behavior. We expect that there is a critical value of m between 0.1 and 0.15 where the dissipation efficiency transitions between increasing and decreasing.

The explanation as to why the dissipation efficiency decreases when m is 0.25 and the frequency increases from 0.3 Hz to 3 Hz correlates with the reason for the steep increase in peak force during that same range of frequency. With more rate-dependency when m is 0.25, as frequency is increased into this range, Branch 1 starts to behave in a more elastic manner, leading to an increase in the peak force, a minimal change in the hysteresis, and a decrease in the dissipation efficiency. This transition is expected to occur as the deformation rate in the material begins to approach the value of $\dot{\gamma}_0$ given in Table 2.1 for each value of m. If higher frequencies were simulated, the dissipation efficiency would likely continue to decrease, and we expect that there would be a similar transition to decreasing dissipation efficiencies for the other m values at sufficiently high loading frequencies. Also, if larger values of m were simulated, this decrease may be even more drastic, and the transition to decreasing dissipation efficiencies would likely occur at lower frequencies.

Non-Equilibrium Shear Modulus

The baseline value of the non-equilibrium shear modulus for Branch 1 ($G_{neq}^{(1)}$) was 580 kPa (Table 1.2), which in this subsection we refer to as G_{neq}. For this parametric study, the baseline value of G_{neq} was multiplied by 0.1, 0.3, 3, and 5. (In Section 2.3.2, the values of $G_{neq}^{(\alpha)}$ for Branches 2, 3, and 4 were varied similarly except that the highest multiplier was 10 instead of 5. Multiplying Branch 1's G_{neq} by anything greater than 5 resulted in a numerically unstable simulation due to the explicit time integration of the flow rule of Branch 1 in the Abaqus subroutine.)

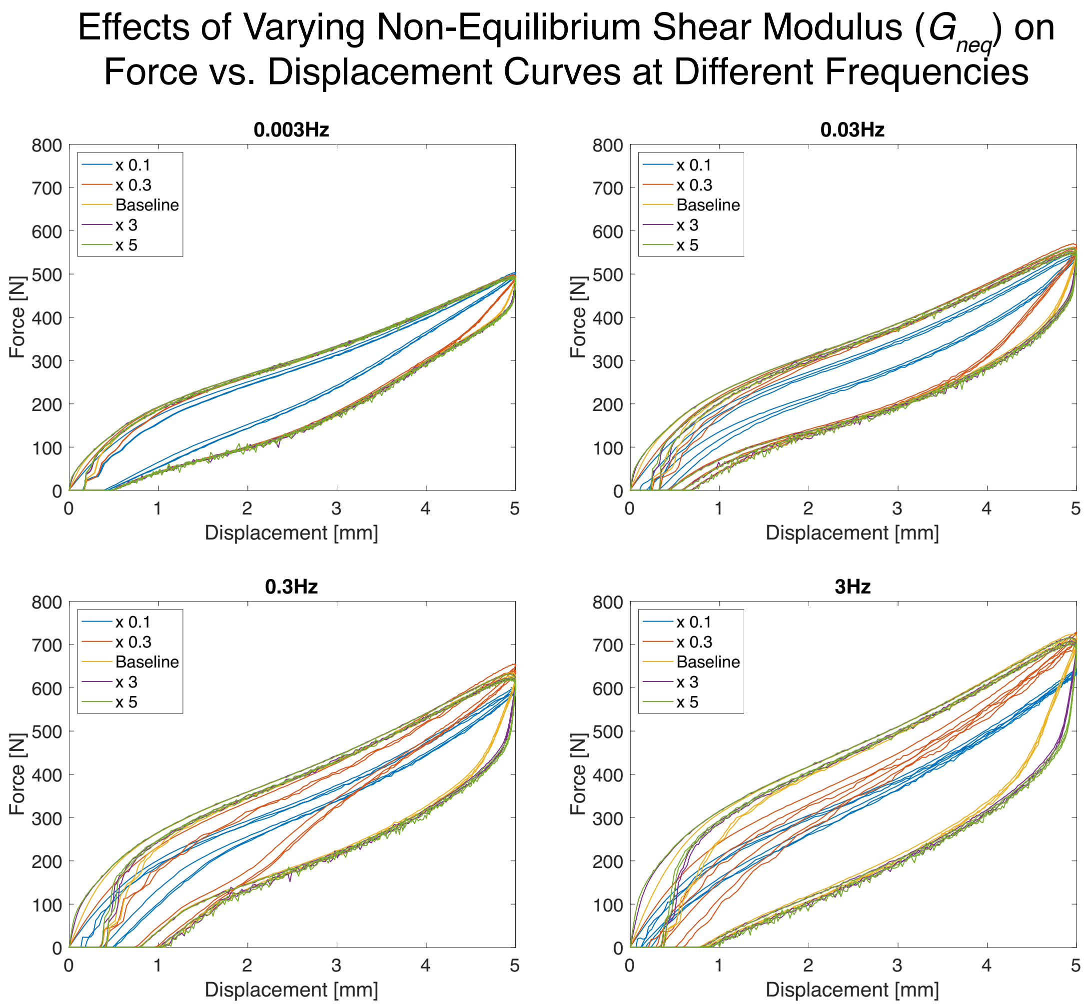

Figure 2.10: Force versus displacement curves during cyclic indentation when varying G_{neq} for Branch 1.

Figure 2.10 presents the effect of varying G_{neq} for Branch 1 on the force versus displacement curves for each loading frequency. As the value of G_{neq} decreases, the hysteresis loops become narrower for each frequency. This is more evident at the elevated frequencies of 0.3 Hz and 3 Hz, where the curves corresponding to when G_{neq} is multiplied by 0.1 and 0.3 are different shapes than the baseline – i.e., the top of the hysteresis loops where the indenter displacement is greatest become thinner. However, the maximum forces remain nearly constant as G_{neq} varies at each frequency. Figure 2.11(left) clearly shows how close in value the peak forces are to each other at each frequency as G_{neq} varies. The outlier is when G_{neq} is multiplied by 0.1 at 0.3 Hz and 3 Hz. These two points are also when the force

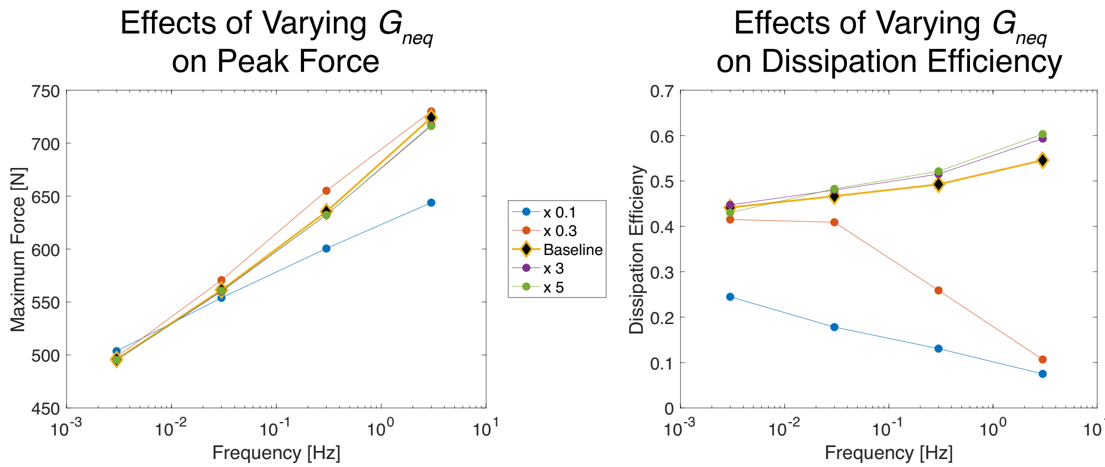

Figure 2.11: Peak forces and dissipation efficiencies as a function of frequency during cyclic indentation when varying G_{neq} for Branch 1.

versus displacement curves transition to a different shape than the baseline. Similar to the parametric study of m, the steady increase in peak forces as the frequencies increase are expected.

The dissipation efficiency does not follow the same trend as the peak forces (Figure 2.11(right)). Although the dissipation efficiencies are close in value for all frequencies when G_{neq} is at its baseline and increased by multiplying by 3 and 5, the dissipation efficiencies at the lower G_{neq} values are significantly different. The higher three G_{neq} values have an increase of dissipation efficiency as the frequency increases, while the other two values of G_{neq} have a decrease of dissipation efficiency as the frequency increases. When G_{neq} is multiplied by 0.1, the value of the dissipation efficiency at 0.003 Hz is approximately 0.2 smaller than the others at the same frequency. Also, at 3 Hz, there is a difference of approximately 0.5 between the dissipation efficiencies of the lower two values of G_{neq} and the dissipation efficiencies of the other three values of G_{neq}.

As G_{neq} decreases, the dissipation efficiency decreases, which stems from the decrease in the contribution of Branch 1 to the hysteresis. The other three non-equilibrium branches still have the tendency to stiffen the material at higher frequencies, which along with the decrease in hysteresis as G_{neq} decreases, leads to the decrease in the dissipation efficiency. Note that for the lowest case of G_{neq} and the highest frequency, the response is very nearly elastic with only a small amount of hysteresis and hence the lowest dissipation efficiency among the cases considered. When increasing its value of G_{neq} above the baseline value, Branch 1 contributes more to the hysteresis and to the maximum force, but these contributions are small and together lead to only a modest increase in the dissipation efficiency. These observations signify that within a certain range, the parameter G_{neq} has a minimal impact on the material response.

2.3.2 Branches 2, 3, and 4

Unlike non-equilibrium Branch 1, which involves non-Newtonian rheological behavior, non-equilibrium Branches 2, 3, and 4 are Newtonian. Hence, we discuss them together and carry out parametric studies on each of their respective non-equilibrium shear moduli $G_{neq}^{(\alpha)}$. The baseline values of $G_{neq}^{(\alpha)}$ for Branch 2, Branch 3, and Branch 4, were 90 kPa, 80 kPa, and 50 kPa, respectively (Table 1.2). The values of G_{neq} (again dropping the superscript for brevity) for each branch were multiplied by 0.1, 0.3, 3, and 10 for each of their respective parametric studies. The graphs of the force versus displacement curves of each branch are included in Appendix A.

Figure 2.12 displays the peak forces and dissipation efficiencies as a function of frequency for all three Newtonian branches for easy comparison of the relevant data. There are two significant elements in Figure 2.12: (1) For cases in which G_{neq} is increased above the baseline, as frequency is increased, there is a drastic increase in peak force for each branch around a certain transition frequency, most evident when G_{neq} is multiplied by 10. (2) For cases in which G_{neq} is increased above the baseline, there is a peak value of dissipation efficiency around a certain frequency (again most evident when G_{neq} is multiplied by 10) followed by a transition period as frequency is further increased, in which the order of the values of dissipation efficiency flip in relation to the ordered values of G_{neq} for each branch. This means that before the transition period, the dissipation efficiencies increased as the

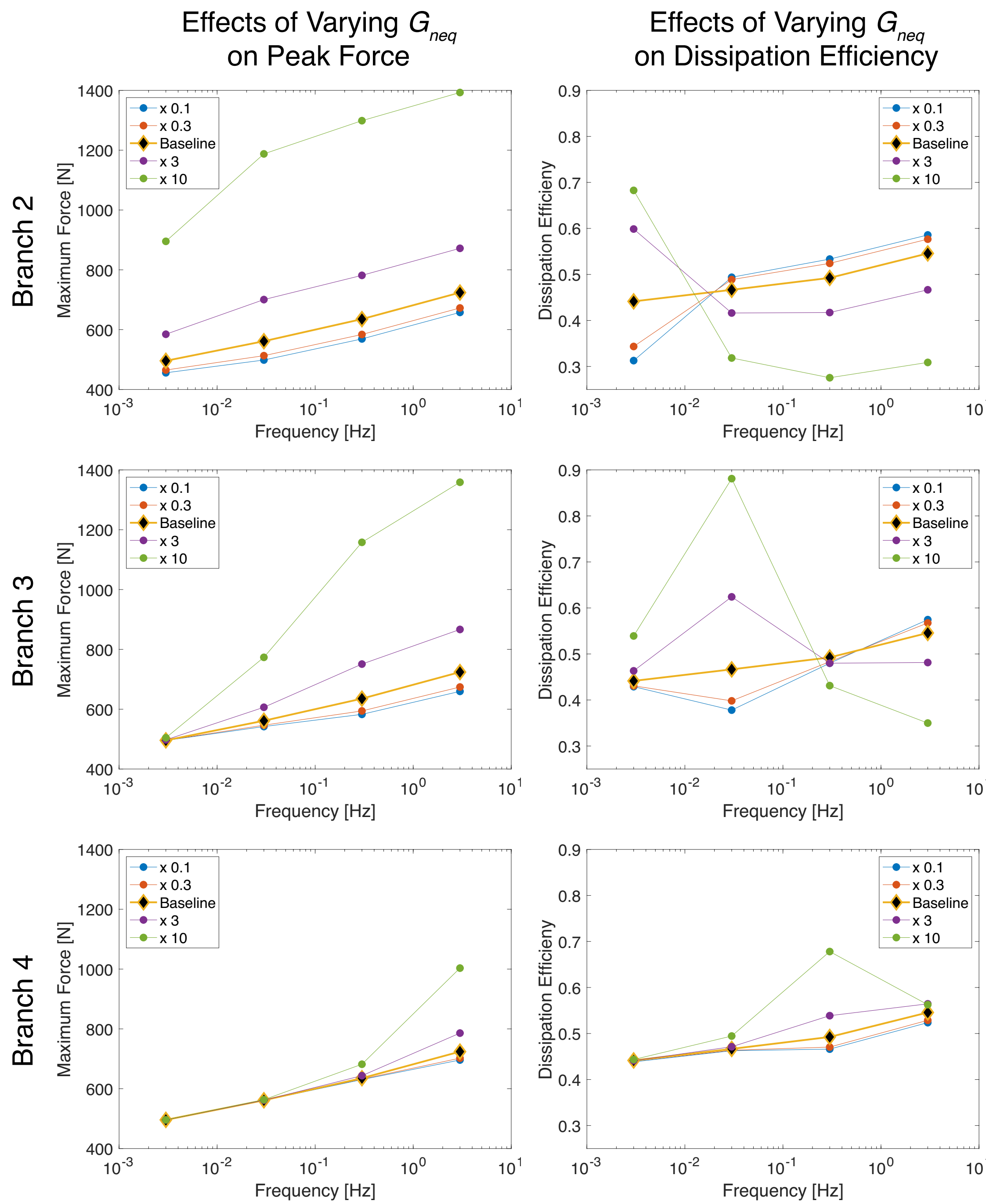

Figure 2.12: Peak forces and dissipation efficiencies as a function of frequency during cyclic indentation when varying G_{neq} for Branches 2, 3, and 4.

value of G_{neq} increased, and for frequencies above the transition, the dissipation efficiencies decreased as the value of G_{neq} increased. These two key observations are reversed for cases in which G_{neq} is decreased relative to the baseline.

Branch 3 clearly demonstrates both of the above elements. The drastic increase in peak force occurs between loading frequencies of 0.03 Hz and 0.3 Hz as the slope between those two data points is steeper than the slopes between the other points for values of G_{neq} that are increased above the baseline. The peak value of dissipation efficiency happens at 0.03 Hz with the most notable peak value close to 0.9 for the highest value of G_{neq} considered. From 0.03 Hz to 0.3 Hz (same frequency transition range as for the increase in peak force), the dissipation efficiency values flip.

For Branch 2, the steepest increase in peak force for elevated values of G_{neq} happens when the frequency changes from 0.003 Hz to 0.03 Hz. The transition of the dissipation efficiencies also happen between those two frequencies. As for Branch 4, the steepest increase in peak force for elevated values of G_{neq} was between 0.3 Hz to 3 Hz, and the peak dissipation efficiency occurred at 0.3 Hz.

Branches 2 and 4 are missing some elements exhibited by Branch 3. In Branch 2, there is no visible peak in the dissipation efficiency similar to the ones in Branches 3 and 4. However, based on the observations with the other branches, if a frequency of one order of magnitude lower were tested (0.0003 Hz), we expect a peak in the dissipation efficiency to be evident. Similarly with Branch 4, there was no transition period where the dissipation values flipped as in Branches 2 and 3. However, if a frequency of one order of magnitude higher were tested (30 Hz), we expect that a transition of the dissipation efficiency would be observed. At 3 Hz for Branch 4, the dissipation efficiencies at all values of G_{neq} do converge around 0.55, suggesting that there would be a transition at a higher frequency.

Figure 2.12 illustrates that there is a correlation between the substantial change in peak force and the transition period in the dissipation efficiencies. As explained in Section 1.2, Branches 2, 3, and 4 are Newtonian branches that are each targeted to a certain characteristic strain rate, particularly to strain rates of $10^{-1}\,\mathrm{s}^{-1}$, $10^{0}\,\mathrm{s}^{-1}$, and $10^{1}\,\mathrm{s}^{-1}$, respectively [34]. To make this more precise, one may think of the Newtonian branches as corresponding to certain characteristic time-scales, particularly to time-scales of 50 s, 2 s, and 0.1 s for

Branches 2, 3, and 4 (Table 1.2) and hence to characteristic frequencies of 1/(50 s) = $0.02\,s^{-1}$, 1/(2 s) = $0.5\,s^{-1}$, 1/(0.1 s) = $10\,s^{-1}$, respectively. As a result, the pattern of the steep increase in peak force at certain transition frequencies observed in the simulations corroborates with the material model. The characteristic frequency of Branch 2 is $0.02\,s^{-1}$, so the increase in peak force occurs when the frequency is increased from 0.003 Hz to 0.03 Hz. This indicates that Branch 2 contributes more to the force level once the frequency has been increased beyond its characteristic frequency. Then, Branch 3 begins to contribute more near its characteristic frequency, which is an order of magnitude higher than Branch 2's ($0.5\,s^{-1}$), exhibiting the steep increase between 0.03 Hz to 0.3 Hz. Lastly, Branch 4 becomes more prevalent near frequencies with magnitudes around $10\,s^{-1}$, thus beginning to display its significant increase in peak force as the loading frequency is increased from 0.3 Hz to 3 Hz.

In reference to the transitions in the dissipation efficiencies, this model indicates that as the loading frequency is increased beyond a branch's characteristic frequency, increasing the non-equilibrium shear modulus G_{neq} of that branch decreases the material's ability to dissipate energy. This may be rationalized as follows. When a given branch is cyclically loaded below its characteristic frequency, the corresponding "dashpot" in Figure 1.1 has sufficient time to continuously relax, and hence that branch does not appreciably contribute to either the peak force or hysteresis. When that branch is cyclically loaded near its characteristic frequency, the corresponding "dashpot" flows and contributes substantially to the hysteresis. When the branch is cyclically loaded above its characteristic frequency, the corresponding "dashpot" does not have time to flow and behaves in a "frozen" manner, leading to the branch to behave in a nearly elastic manner and contribute negligbly to the hysteresis but substantially to the force level. Because the parameter G_{neq} scales the contribution of a given branch to the total Cauchy stress, increasing this parameter increases the branch's contribution to the total hysteresis near its characteristic frequency and decreases its ability to contribute to energy dissipation above its characteristic frequency. As such, by increasing one branch's G_{neq}, the effect of that branch on the material behavior becomes more apparent around its corresponding frequency. Thus, with an increasing G_{neq}, a decrease in dissipation efficiency is expected once each branch traverses its corresponding frequency. The opposite effect is true when the non-equilibrium shear modulus G_{neq} for a given branch is decreased instead of increased.

Chapter 3

Application to Shoe Midsoles

The second part of this study focused on the application of the constitutive model to cyclic indentation tests of a flat, circular indenter on a shoe midsole made of EVA foam (Section 3.1). We completed two parametric studies, through Abaqus simulations, focusing on the effect of the loading frequency (Section 3.2) of the cyclic indentation and the effect of the position (Section 3.3) of the indenter in reference to the shoe midsole. As in Chapter 2, the effect of each parametric study was quantified through the maximum force applied and the dissipation efficiency of the foam.

3.1 Simulation Details and Baseline Results

As shown in Figure 3.1, a three-dimensional model was simulated with two components, a cylindrical indenter and a representation of a shoe midsole. The geometry of this particular shoe midsole is from Reebok's Zig line of shoes, and the simulation was configured to fit those dimensions. Reebok's Zig midsole was aptly named to describe the design of the midsole, which has a "zig-zag" geometric pattern, creating multiple "bars" throughout the midsole. Each bar of the midsole was numbered from 1 to 9. The indentation locations considered in this study were bars 4 to 9. This choice was made mostly for convenience because within this part of the midsole, the corresponding bottoms were parallel with the

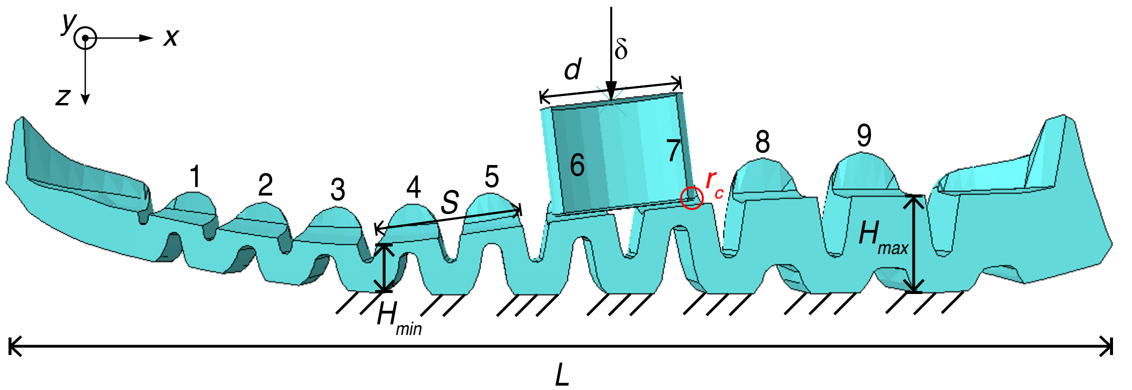

Figure 3.1: Configuration for numerical simulations of cyclic indentation of a shoe midsole with a view cut along the x-z-plane.

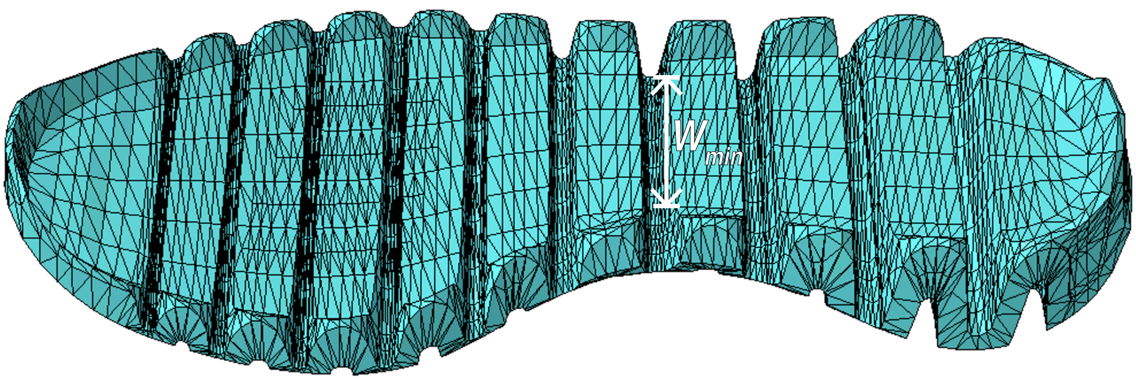

Figure 3.2: Top-view of the shoe midsole geometry and finite-element mesh.

ground, making the application of boundary conditions straightforwad. Thus, the nodes along those bottoms were rigidly bounded in all three directions ($u_x = u_y = u_z = 0$), as shown in Figure 3.1.

The same cylindrical indenter geometry was used in all simulations, so the diameter (d) was set as 40 mm to fit within the minimum width (W_{min}) of the midsole, which was 44 mm. (W_{min} was measured before the top of the midsole starts to curve to transition into the wall as shown in Figure 3.2.) The bottom edge of the cylinder was rounded with a radius (r_c) of 0.6 mm to mitigate potential numerical issues, and the height (h) of the indenter was arbitrarily chosen to be 30 mm.

All simulations were completed using displacement control, and the displacement (δ) of the indenter along the z-direction was prescribed at its reference point. The prescribed movement was a displacement that sinusoidally cycled between 0 mm and 7 mm only along the z direction for all simulations and rotation was prohibited. The indenter completed three cycles of loading onto and unloading off of the foam, imposing uniaxial compression-like deformation in the foam beneath the indenter. A displacement magnitude of 7 mm was selected so an appropriate maximum displacement was achieved regardless of the indenter's position from bars 4 to 9 as the minimum (H_{min}) and maximum (H_{max}) heights were about 13.2 mm and 26.8 mm, respectively (see Figure 3.1).

The contact area of the indenter onto the midsole spanned two bars for every simulation in order to better represent the contact between a portion of a foot with the shoe midsole as well as to maximize the contact area of the indenter. The average length of the span of two bars (S) was 44.7 mm, and the overall length of the midsole from the tip of the toe to the back of the heel (L) was about 30.5 cm (Figure 3.1). For each simulation, the indenter was rotated to be parallel with the two bars being contacted, and this contact between the foam midsole and the indenter was idealized with a friction coefficient of 0.4 in the simulations.

Additional images of the undeformed model are shown in Figure 3.3, presenting more views of the meshed parts. The indenter was idealized as a discrete rigid body and was arbitrarily meshed using 243 Abaqus-R3D4 elements (four-node, three-dimensional, rigid, quadrilateral elements). The entire midsole was meshed using 21,203 Abaqus-C3D10M elements (ten-node, modified, quadratic, tetrahedral elements).

Just as in Chapter 2, all finite-element calculations were performed in Abaqus/Explicit, using the VUMAT subroutine implementation of the constitutive model, and the primary data collected was the reaction force history experienced by the indenter during cyclic indentation on the foam. This information allowed for the comparison of maximum force applied and the dissipation efficiency of the foam, as explained in Section 2.1. Although those quantities are the only results discussed in Sections 3.2 and 3.3, other interesting observations from the simulations were the stress and deformation fields experienced by the midsole during indentation. Figure 3.4 displays relevant contour plots of the designated

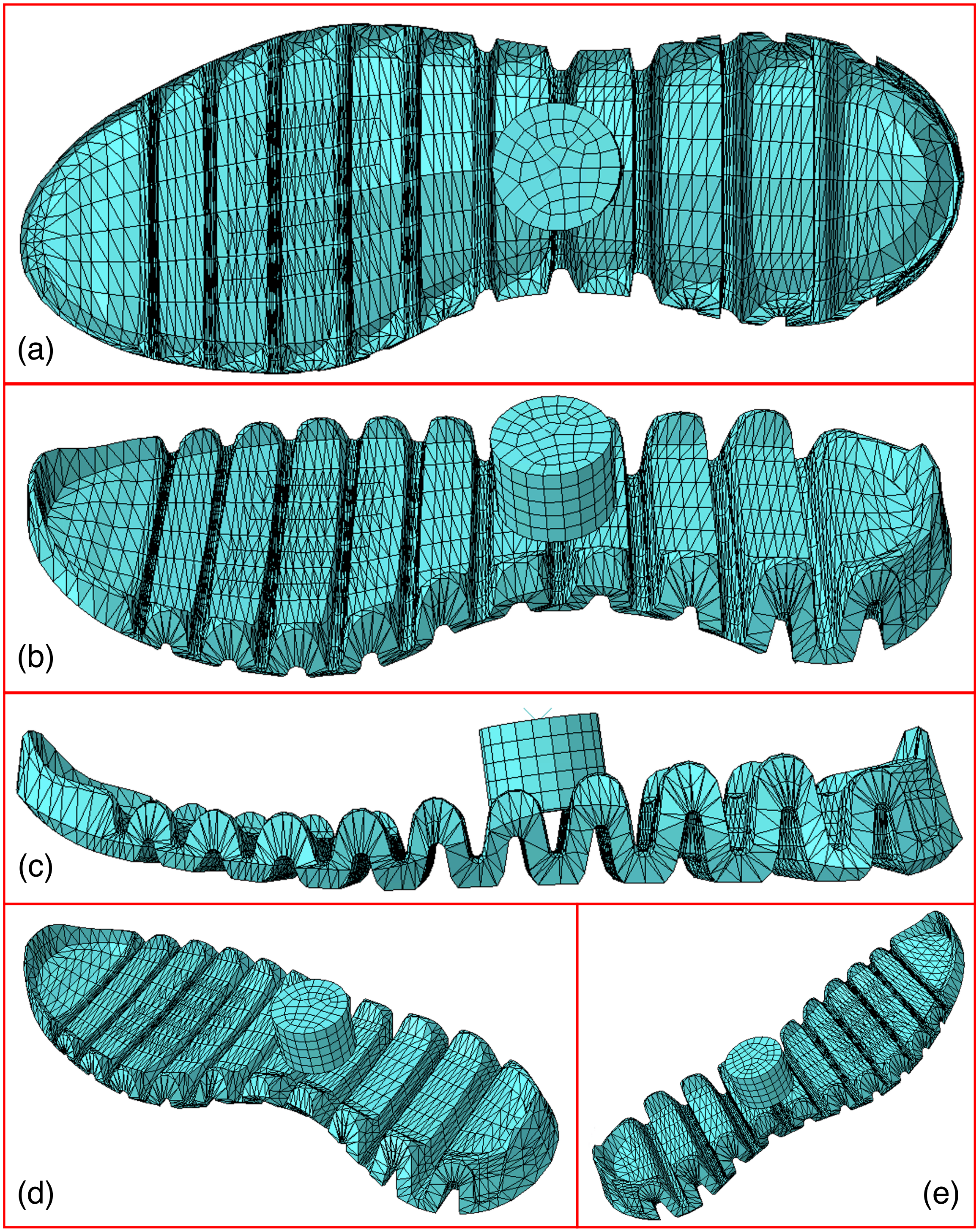

Figure 3.3: Multiple views of the undeformed shoe midsole and indenter geometry and finite-element mesh. (a,b) Top views. (c) Side view. (d,e) Perspective views.

baseline case (the simulation that is involved in both parametric studies), which is when the indenter spanned bars 6 and 7 (as shown in Figure 3.1) with a loading frequency of 3 Hz.

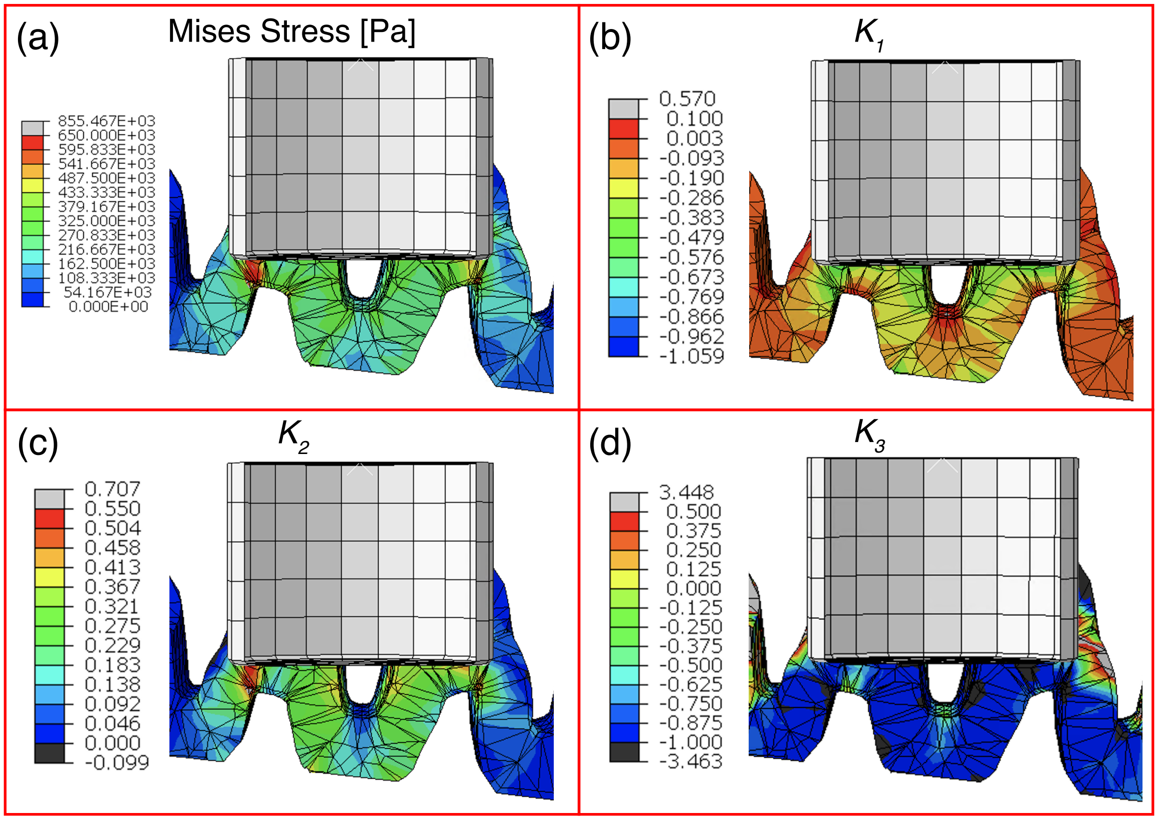

Figure 3.4: Contour plots of the von Mises effective stress and logarithmic strain invariants (K_1, K_2, and K_3) for the baseline case at an indenter displacement of 7 mm onto shoe midsole.

The contour plots are only shown for the baseline case at an indenter displacement of 7 mm to give a general example of the fields that arise in the EVA midsole during the simulations. As shown in Figure 3.4(a), the magnitude of the von Mises effective stress beneath the indenter is on the order of 300-500 kPa. The magnitude of stress is fairly constant for most of the deformed material, but a peak stress does occur by the left corner of the indenter. Contours of the invariants of the logarithmic strain tensor (K_1, K_2, and K_3) are also shown in Figures 3.4(b)-(d). Recall from Section 1.2.1 that K_1 represents the amount of dilatation, $K_2 > 0$ is the magnitude of constant-volume distortion, and $-1 \leq K_3 \leq 1$ represents the mode of constant-volume distortion. In Figure 3.4(b) most of the foam beneath the indenter exhibits a negative volume change, which corresponds with the material being compressed. However, there is some increase of volume at the three areas of curvature where the material experiences bending. For K_2, the contour plot is quite similar to the von

Mises stress field, demonstrating the relation between deviatoric stress and strain. Lastly, the contour plot of K_3 in Figure 3.4(d) is mostly blue, indicating that the value of K_3 is -1, which is the value for simple compression. The exact fields for stress or deformation will differ throughout the parametric studies, but the results of the maximum force applied and the dissipation efficiency encompasses those changes.

3.2 Varying Frequency at One Position

For the first parametric study of cyclic indentation of the shoe midsole, the position of the indenter was fixed to span bars 6 and 7, and the frequency of the cyclic motion of the indenter was varied. The four different values of loading frequencies were 0.003 Hz, 0.03 Hz, 0.3 Hz, and 3 Hz.

Figure 3.5 shows the effect of varying the loading frequency at one position on the force versus displacement curves. (The shakiness of the 3 Hz curve and, to a lesser extent, the other curves in Figure 3.5 is due to the level of mass scaling selected to efficiently run the explicit finite-element calculations but does not significantly affect the overall results.) As the frequency increased, the maximum force experienced by the foam increased. The hysteresis loop and hence the dissipation efficiency also increased with an increase in frequency. These relations are explicitly shown as a function of frequency in Figure 3.6. The maximum force and dissipation efficiency both increase with an increasing magnitude of frequency.

These results agree with our physical intuition for the viscoelastic nature of the foam material because indenting the material to the same displacement magnitude but within different periods of time would mean more force is required to displace the material at a shorter time period compared to displacing the same amount during a longer period of time. Furthermore, with an increasing loading frequency, the dissipation efficiency also increases as more of the non-equilibrium branches contribute to the hysteresis. This result is analogous to what occurred in the baseline cases in Chapter 2.

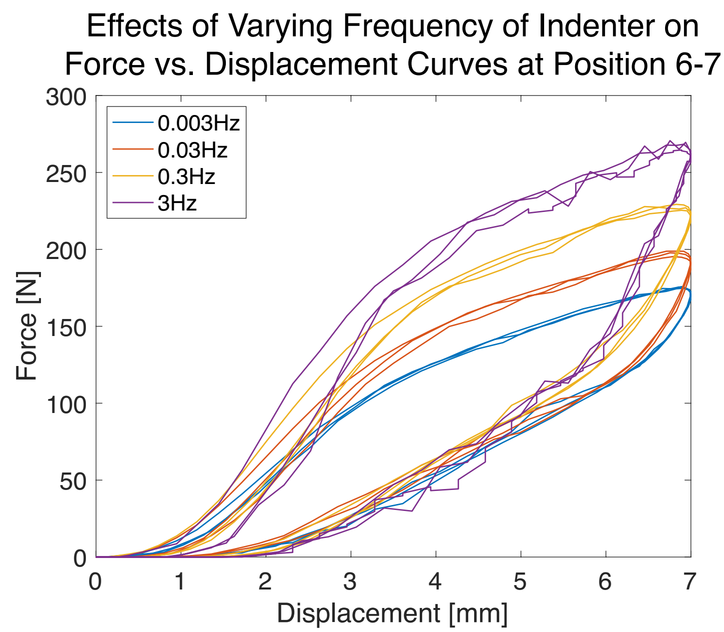

Figure 3.5: Force versus displacement curves during cyclic indentation of a shoe midsole when varying loading frequency at a fixed position.

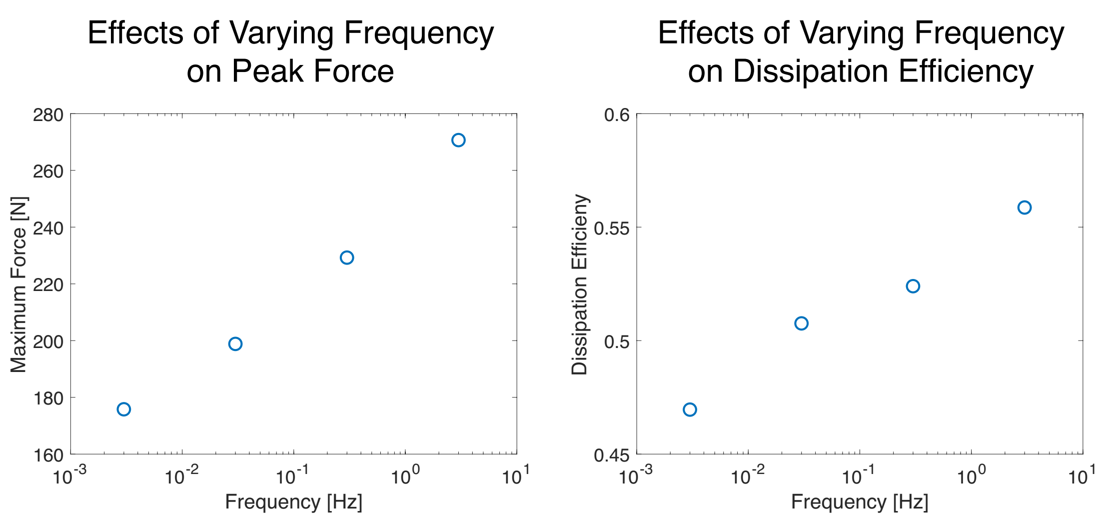

Figure 3.6: Peak forces and dissipation efficiencies as a function of frequency during cyclic indentation of a shoe midsole at a fixed position.

3.3 Varying Position at One Frequency

For the second parametric study of cyclic indentation of the shoe midsole, the loading frequency was fixed at 3 Hz, and the position of the indenter along the midsole was varied. The five different positions considered were when the indenter was in contact with bars 4-5,

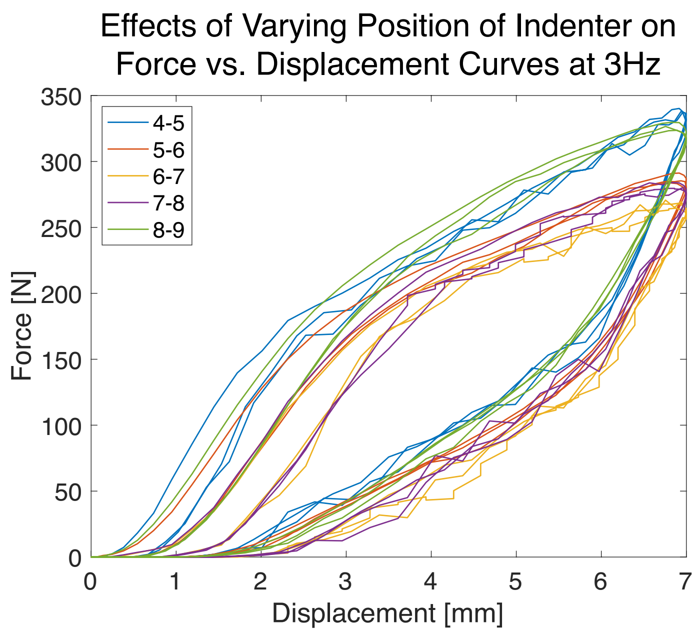

Figure 3.7: Force versus displacement curves during cyclic indentation of a shoe midsole when varying the position of the indenter at 3 Hz.

5-6, 6-7, 7-8, and 8-9.

Figure 3.7 shows the effect of varying the indenter position on the force versus displacement curves with the frequency fixed at 3 Hz . (The shakiness in the simulated curves is again due to mass scaling and does not significantly affect the overall results.) A noticeable feature within this set of simulated curves is that there are three distinguishable tiers of peak forces. The highest maximum force is when the indenter was at positions 4-5 and 8-9. The second highest peak force is when the indenter was at positions 5-6 and 7-8. Lastly, the lowest maximum force is from the 6-7 position.

This is clearly demonstrated in Figure 3.8(left), where the maximum forces at the two end positions are the highest and close in value, and the values decrease going to the lowest peak force at the middle position. However, the dissipation efficiency does not follow the same relation, in fact, it is nearly the inverse. The 6-7 position experiences the lowest maximum force but experiences the highest dissipation efficiency. Moreover, the end positions (4-5 and 8-9) had lower dissipation efficiencies but still of similar values to each other. Position 5-6

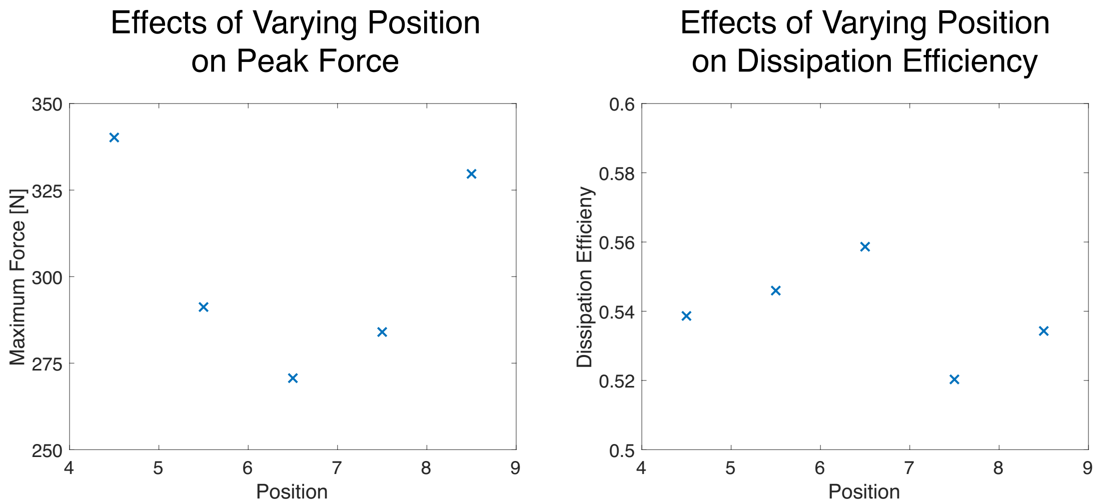

Figure 3.8: Peak forces and dissipation efficiencies as a function of position during cyclic indentation of a shoe midsole at 3 Hz.

remains within the middle of the range for dissipation efficiency, just as it did for the peak forces. Position 7-8 is the outlier that does not follow this inverse relation of the dissipation efficiency to the peak force. If that relation was followed, the expected outcome for the 7-8 position dissipation efficiency would be of similar value to the 5-6 position, but as shown in Figure 3.8(right), this is not the case. In fact, the dissipation efficiency at position 7-8 is the lowest. In Figure 3.7, one can see that although the 7-8 curve reaches a similar peak force as the 5-6 curve, the loading curve of the stabilized hysteresis loop for position 7-8 follows the same path as position 6-7, resulting in a lower dissipation efficiency compared to both position 5-6 and position 6-7.

The main reason for this outcome is due to the shape of the midsole, which affects the dominant mode of deformation of each bar and the magnitude of deformation that each bar experiences. One feature of the midsole is that the height of each bar increases going from bar 4 to bar 9. Since the maximum indenter displacement is the same at all positions, the magnitude of deformation decreases going from bar 4 to bar 9. A second feature is that the cavities within bars 4 to 7 maintain the same ratio of empty space to foam, however the cavities in bars 8 and 9 are much less prevalent. When there is a significant cavity, as in bars

4 to 7, the bars can be seen as being composed of two vertical beams. As such, bending of these beams is the more dominant mode of deformation during the displacement of the indenter. When there are less prevalent cavities, as in bars 8 and 9, the bar more resembles a block of foam, prompting a compression-dominant deformation.

Since positions 4-5 to 6-7 all experience bending-dominant deformation, the decreasing peak force and increasing dissipation efficiency are directly related to the decrease in the imposed deformation magnitude as the indenter moves from position 4-5 to 6-7. Similar to the relation demonstrated in the parametric study of J_{min} (Section 2.2.2), a section of the midsole subjected to a higher deformation magnitude (e.g. position 4-5) would cause the material to become stiffer compared to a section subjected to a lower deformation magnitude (e.g. position 6-7), causing a higher peak force but lower dissipation efficiency. As the position of the indenter transitions from 6-7 to 7-8, the bars also transition in the dominant mode of deformation. In position 7-8, bar 7 is more bending-dominant while bar 8 is more compression-dominant. This combination of deformation types may be why the loading curve of position 7-8 follows the loading curve of position 6-7 (bending-dominant behavior) but reaches a higher peak force (compression-dominant behavior), thus causing a decrease in the dissipation efficiency. In position 8-9, both bars are compression-dominant, resulting in the increase in peak force. The dissipation efficiency increases as well because the state of deformation in the midsole beneath the indenter is similar to the block of foam that we considered in Chapter 2.

Chapter 4

Conclusion

4.1 Summary

In this thesis, we conducted two types of parametric studies utilizing a nonlinear, large-deformation, viscoelastic constitutive model. The first type of parametric studies focused on the material properties that appear in the constitutive model, and the second type of parametric studies was focused on the application of the model to a shoe midsole. An axisymmetric model based on Reebok's experimental procedure was used for the studies on material properties, and a three-dimensional model based on the geometry of Reebok's Zig midsole was used for the studies on a shoe midsole.

Both equilibrium and non-equilibrium material properties of the constitutive model were studied at four different loading frequencies (0.003 Hz, 0.03 Hz, 0.3 Hz, 3 Hz). Similar results arose when examining the effect of the ground-state shear (G_0) and bulk (B) moduli and the volumetric locking value (J_{min}). When the ratio of (G_0/B) and J_{min} increased, the material became stiffer, which increased the peak force while the dissipation efficiency decreased. However, the effect of increasing G_0 and B caused the material to respond in a more elastic manner and increased the entire force versus displacement curves, while J_{min} only affected the large deformation response, which still allowed a discernible amount of energy to be dissipated. Also, the dissipation efficiency depended nearly linearly on J_{min} for all frequencies.

The non-equilibrium shear moduli for each branch ($G_{neq}^{(\alpha)}$) were the main parameters of interest when studying the non-equilibrium parameters. For all four branches, increasing their respective G_{neq} made the branches contribute more to the hysteresis and maximum force. For Branch 1, these contributions were small once the non-equilibrium shear modulus was sufficiently large, signifying that within a certain range, G_{neq} had a minimal impact on the material response. For the other three branches, the increase in G_{neq} affected the material behavior more prominently around their corresponding characteristic frequencies as the contribution to the total hysteresis increased near each branch's characteristic frequency. Also, for loading frequencies above their characteristic frequencies, each branch continued to contribute in attaining higher maximum forces as G_{neq} increased, but decreased the material's ability to dissipate energy.

The strain-rate sensitivity exponent (m) for Branch 1 was also examined. The material behavior was dependent on the value of m because when $m = 0.1$, Branch 1's contribution to the material's hysteresis remained nearly constant as the frequency increased, while the peak force increased, leading to a decrease in dissipation efficiency. However, when m was 0.15 and above, a higher maximum force was accompanied by sufficiently large increase in the amount of hysteresis, yielding a higher dissipation efficiency with increasing frequency. Once m was 0.25, increasing to a frequency range above 0.3 Hz, Branch 1 started to behave more elastically. The combination of all these observations demonstrated how the material behaved as Branch 1 became more rate-dependent (i.e., m increased).

When the constitutive model was applied to the midsole of a shoe, two parameters were varied, the loading frequency and the position of the indenter. As the frequency increased when the indenter was at a fixed position, the peak force and dissipation efficiency also increased. As the position of the indenter moved throughout the midsole, the geometry of the midsole affected the material response. When the bars of the midsole were bending-dominant, a decrease in the magnitude of deformation led to a decrease in the peak force but an increase in the dissipation efficiency. As the indenter transitioned from displacing bending-dominant regions to compression-dominant regions, there was an initial decrease in dissipation efficiency, however the peak force increased. The dissipation efficiency increased, and the peak force continued to increase once the displaced region was all compression-dominant.

4.2 Future Directions

While progress has been made, there are many directions for future work. Performing another parametric study of the strain-rate sensitivity exponent (m) for Branch 1 with a wider range of m and frequency would allow for our predictions stated in Section 2.3.1 to be confirmed or denied. Also, another study that increases m by smaller increments would help to find the critical value of m where the dissipation efficiency transitions between increasing and decreasing. The parametric study focused on G_{neq} for the Newtonian branches is a second study that could be repeated with a wider range of frequencies. By expanding the frequency range, the missing elements, such as a visual peak of dissipation efficiency for Branch 2 and the transition of the dissipation efficiency values for Branch 4, can be presented.

Both parametric studies for the shoe midsole can also be expanded. The study that varied loading frequency can be performed at multiple positions to verify the observation that increasing frequency increases both peak force and dissipation efficiency, no matter the region of the midsole being displaced. Moreover, the study varying position can have smaller increments in the change of position of the indenter relative to the midsole so that the indenter would be centered at one bar instead of between two bars. The shape of the indenter could also be changed, such as elongating the contact area to span more than two bars. Lastly, these parametric studies could be applied to many different designs of shoe midsoles or to full shoe assemblies including the other components of a shoe to see how each performs in terms of peak forces and dissipation efficiencies within a range of frequencies.

Appendix A

Force Versus Displacement Curves for Parametric Studies Involving Non-Equilibrium Newtonian Branches

The following figures display the force versus displacement curves for Branches 2, 3, and 4.

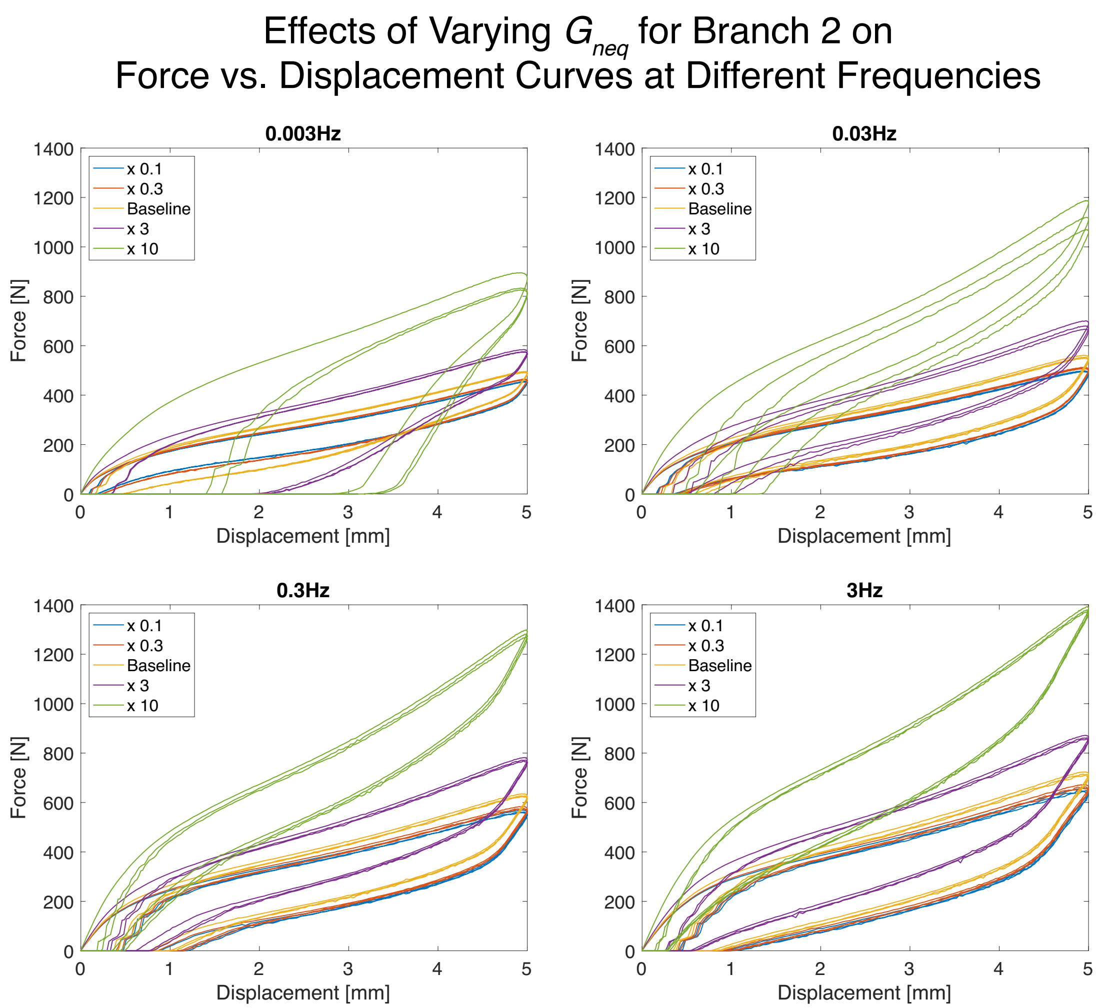

Figure A.1: Force versus displacement curves during cyclic indentation when varying G_{neq} for Branch 2.

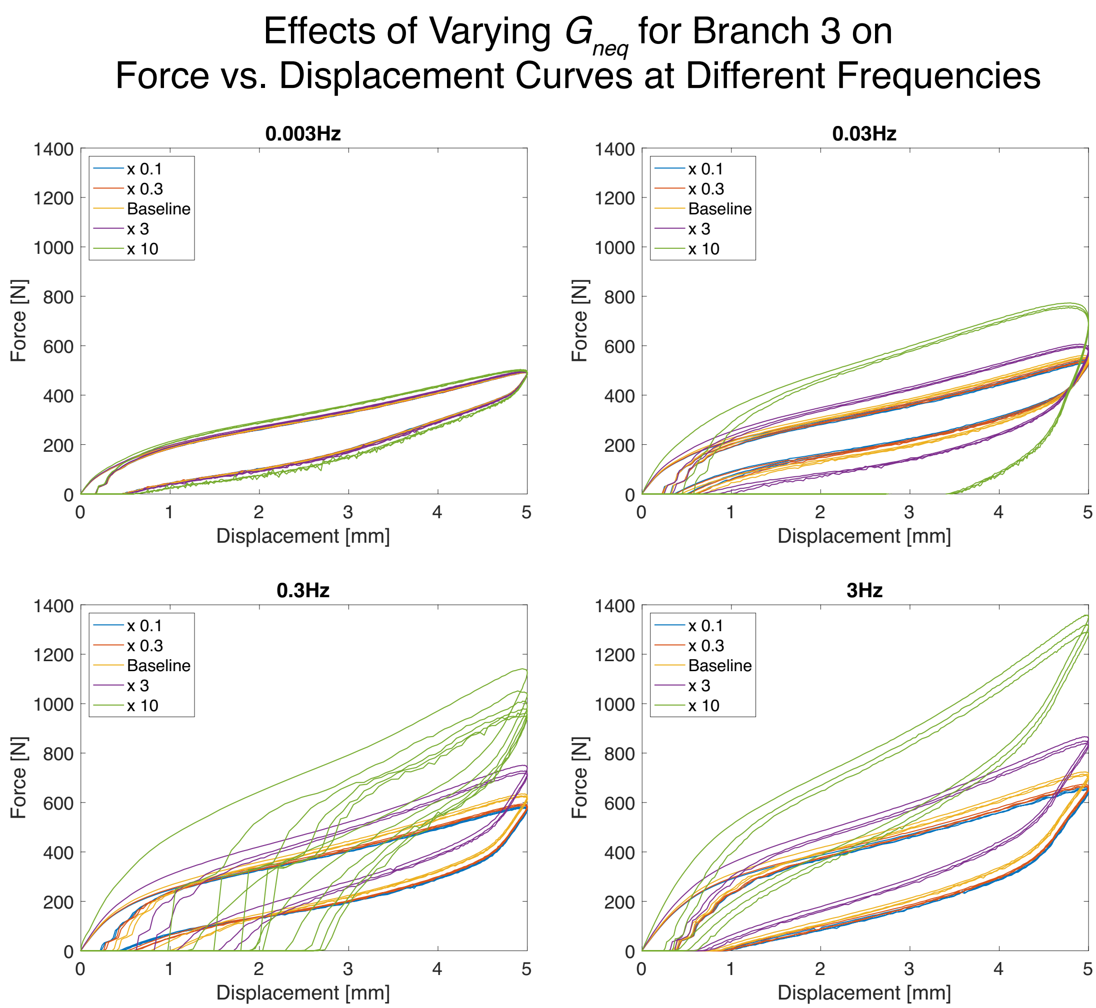

Figure A.2: Force versus displacement curves during cyclic indentation when varying G_{neq} for Branch 3.

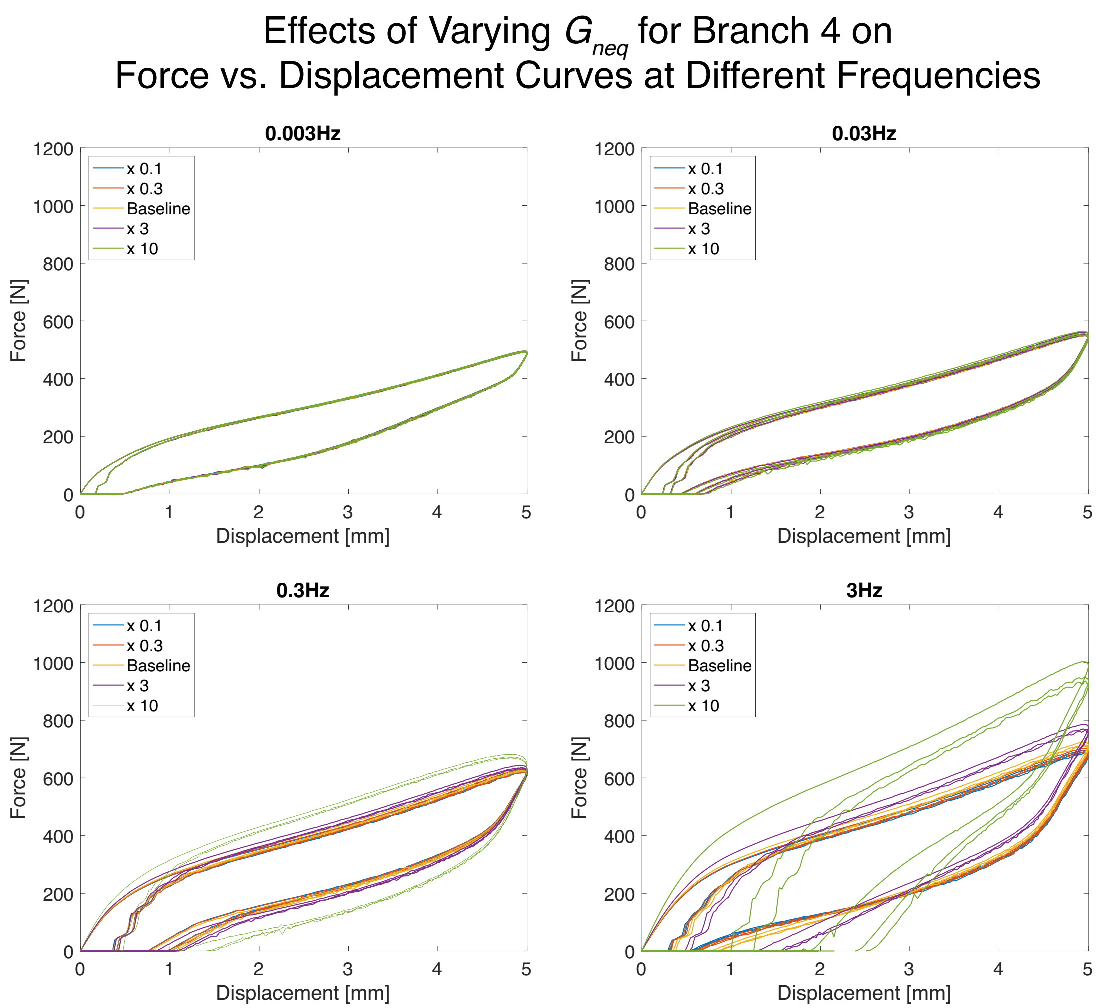

Figure A.3: Force versus displacement curves during cyclic indentation when varying G_{neq} for Branch 4.

Bibliography

[1] R. Verdejo and N. Mills. Performance of EVA foam in running shoes. In S. Ujihashi and S. Haake, editors, *The engineering of sport 4*, pages 580–587. Blackwell Science, 2002.

[2] N. Mills, C. Fitzgerald, A. Gilchrist, and R. Verdejo. Polymer foams for personal protection: cushions, shoes and helmets. *Composites Science and Technology*, 63: 2389–2400, 2003. doi: 10.1016/S0266-3538(03)00272-0.

[3] M.R. Shariatmadari, R. English, and G. Rothwell. Effects of temperature on the material characteristics of midsole and insole footwear foams subject to quasi-static compressive and shear force loading. *Materials & Design*, 37:543–559, 2012. doi: 10.1016/j.matdes.2011.10.045.

[4] R.W. Ogden. Large deformation isotropic elasticity: On the correlation of theory and experiment for compressible rubberlike solids. *Proceedings of the Royal Society of London. Series A, Mathematical and Physical Sciences*, 328:567–583, 1972. doi: 10.1098/rspa.1972.0096.

[5] B. Storakers. On material representation and constitutive branching in finite compressible elasticity. *Journal of the Mechanics and Physics of Solids*, 34:125–145, 1986. doi: 10.1016/0022-5096(86)90033-5.

[6] S. Jemiolo and S. Turteltaub. Parametric model for a class of foam-like isotropic

hyperelastic materials. *Journal of Applied Mechanics*, 67:248–254, 2000. doi: 10.1115/1.1305277.

[7] N.J. Mills and A. Gilchrist. Modelling the indentation of low density polymer foams. *Cellular Polymers*, 19:389–412, 2000.

[8] C. Briody, B. Duignan, S. Jerrams, and J. Tiernan. The implementation of a visco-hyperelastic numerical material model for simulating the behaviour of polymer foam materials. *Computational Material Science*, 64:47–51, 2012. doi: 10.1016/j.commatsci.2012.04.012.

[9] W. Chen, Z.-X. Lu, B. Pan, J.-H. Guo, and Y.-J. Li. Nonlinear behavior of bumper foams under uniaxial compressive cyclic loading. *Materials and Design*, 35:491–497, 2012. doi: 10.1016/j.matdes.2011.09.042.

[10] M. L. Ju, S. Mezghani, H. Jmal, R. Dupuis, and E. Aubry. Parameter estimation of a hyperelastic constitutive model for the description of polyurethane foam in large deformation. *Cellular Polymers*, 32:21–40, 2013. doi: 10.1177/026248931303200102.

[11] P. J. Blatz and W. L. Ko. Application of finite elastic theory to the deformation of rubbery materials. *Transactions of the Society of Rheology*, 6:223–251, 1962. doi: 10.1122/1.548937.

[12] J. G. Murphy. Strain energy function for a Poisson power law function in simple tension of compressible hyperelastic materials. *Journal of Elasticity*, 60:151–164, 2000. doi: 10.1023/A:1010843015909.

[13] J. Ciambella and G. Saccomandi. A continuum hyperelastic model for auxetic materials. *Proceeding of the Royal Society of London A*, 470:20130691, 2014. doi: 10.1098/rspa.2013.0691.

[14] A.K. Landauer, X. Li, C. Franck, and D.L. Henann. Experimental characterization and hyperelastic constitutive modeling of open-cell elastomeric foams. *Journal of the Mechanics and Physics of Solids*, 133:103701, 2019.

[15] M. Danielsson, D.M. Parks, and M.C. Boyce. Constitutive modeling of porous hyperelastic materials. *Mechanics of Materials*, 36:347–258, 2004. doi: 10.1016/S0167-6636(03)00064-4.

[16] O. Lopez-Pamies and P. Ponte Castañeda. Homogenization-based constitutive models for porous elastomers and implications for microscopic instabilities: I – Analysis. *Journal of the Mechanics and Physics of Solids*, 55:1677–1701, 2007. doi: 10.1016/j.jmps.2007.01.007.

[17] O. Lopez-Pamies and P. Ponte Castañeda. Homogenization-based constitutive models for porous elastomers and implications for microscopic instabilities: II – Results. *Journal of the Mechanics and Physics of Solids*, 55:1702–1728, 2007. doi: 10.1016/j.jmps.2007.01.008.

[18] B. Shrimali, V. Lefèvre, and O. Lopez-Pamies. A simple explicit homogenization solution for the macroscopic elastic response of isotropic porous elastomers. *Journal of the Mechanics and Physics of Solids*, 122:364–380, 2019. doi: 10.1016/j.jmps.2018.09.026.

[19] V. Shulmeister, M. W. D. van der Burg, E. van der Giessen, and R. Marissen. A numerical study of large deformations of low-density elastomeric open-cell foams. *Mechanics of Materials*, 30:125–140, 1998. doi: 10.1016/S0167-6636(98)00033-7.

[20] Y. Wang and A. M. Cuitiño. Three-dimensional nonlinear open-cell foams with large deformations. *Journal of the Mechanics and Physics of Solids*, 48:961–988, 2000. doi: 10.1016/S0022-5096(99)00060-5.

[21] A.D. Brydon, S.G. Bardenhagen, E A. Miller, and G.T. Seidler. Simulation of the densification of real open-celled foam microstructures. *Journal of the Mechanics and Physics of Solids*, 53:2638–2660, 2005. doi: 10.1016/j.jmps.2005.07.007.

[22] T. Sabuwala and G. Gioia. Skeleton-and-bubble model of polyether-polyurethane elastic open-cell foams for finite element analysis at large deformations. *Journal of the Mechanics and Physics of Solids*, 61:886–911, 2013. doi: 10.1016/j.jmps.2012.10.007.

[23] L. Gong and S. Kyriakides. Compressive response of open cell foams. Part II: Initiation and evolution of crushing. *International Journal of Solids and Structures*, 42:1381–1399, 2005. doi: 10.1016/j.ijsolstr.2004.07.024.

[24] Z. Guo, F. Caner, X. Peng, and B. Moran. On constitutive modelling of porous neo-hookean composites. *Journal of the Mechanics and Physics of Solids*, 56:2338–2357, 2008. doi: 10.1016/j.jmps.2007.12.007.

[25] Y. Chen, W. Guo, P. Yang, J. Zhao, Z. Guo, L. Dong, and Z. Zhong. Constitutive modeling of neo-Hookean materials with spherical voids in finite deformation. *Extreme Mechanics Letters*, 24:47–57, 2018. doi: 10.1016/j.eml.2018.08.007.

[26] Y. Anani and Y. Alizadeh. Visco-hyperelastic constitutive law for modeling of foam's behavior. *Materials and Design*, 32:2940–2948, 2011. doi: 10.1016/j.matdes.2010.11.010.

[27] L.M. Yang and V.P.W. Shim. A visco-hyperelastic constitutive description of elastomeric foam. *International Journal of Impact Engineering*, 30:1099–1110, 2004. doi: 10.1016/j.ijimpeng.2004.03.011.

[28] M.L. Ju, H. Jmal, R. Dupuis, and E. Aubry. Visco-hyperelastic constitutive model for modeling the quasi-static behavior of polyurethane foam in large deformation. *Polymer Engineering and Science*, 55:1795–1804, 2015. doi: 10.1002/pen.24018.

[29] A. Kossa and S. Berezvai. Visco-hyperelastic characterization of polymeric foam materials. *Materials Today: Proceedings*, 3:1003–1008, 2016. doi: 10.1016/j.matpr.2016.03.037.

[30] J.S. Bergström. Advanced finite element modeling of polymer foam components. In *Proceedings of the ABAQUS Users' Conference*, pages 81–94, 2006.

[31] B. Markert. A biphasic continuum approach for viscoelastic high-porosity foams: Comprehensive theory, numerics, and application. *Archives of Computational Methods in Engineering*, 15:371–446, 2008. doi: 10.1007/s11831-008-9023-0.

[32] N. Koprowski-Theiß, M. Johlitz, and S. Diebels. Modelling of a cellular rubber with nonlinear viscosity functions. *Experimental Mechanics*, 51:749–765, 2011. doi: 10.1007/s11340-010-9376-9.

[33] N. Koprowski-Theiß, M. Johlitz, and S. Diebels. Compressible rubber materials: experiments and simulations. *Archive of Applied Mechanics*, 82:1117–1132, 2012. doi: 10.1007/s00419-012-0616-6.

[34] X. Li, J. Tao, A.K. Landauer, C. Franck, and D.L. Henann. Large-deformation constitutive modeling of viscoelastic foams: Application to a closed-cell foam material. *Journal of the Mechanics and Physics of Solids*, 161:104807, 2022.

[35] J.C. Criscione, J.D. Humphrey, A.S. Douglas, and W.C. Hunter. An invariant basis for natural strain which yields orthogonal stress response terms in isotropic hyperelasticity. *Journal of the Mechanics and Physics of Solids*, 48:2445–2465, 2000. doi: 10.1016/S0022-5096(00)00023-5.

[36] L. Anand, N.M. Ames, V. Srivastava, and S.A. Chester. A thermo-mechanically coupled theory for large deformations of amorphous polymers. Part I: Formulation. *International Journal of Plasticity*, 25:1474–1494, 2009. doi: 10.1016/j.ijplas.2008.11.004.